



Aerodynamic shape optimization by continually moving ROM

Li Li Zhou ^{a,*}, Li Jin Jiu ^a, Zhang Jun ^b, Lu Kuan ^a, Yuan Mei Ni ^a



^a School of Mechatronic Engineering, North University of China, Taiyuan, 030051, China

^b Department of Mathematic, Taiyuan University, Taiyuan, 030001, China

ARTICLE INFO

Article history:

Received 31 January 2019

Received in revised form 23 November 2019

Accepted 22 January 2020

Available online 27 January 2020

Communicated by Dionysios Angelidis

Keywords:

Aerodynamic

Shape optimization

Reduced order model

Moving search

Taylor expansion

Parameterization

ABSTRACT

This study presents a multi-round shape optimization method based on the aerodynamic reduced order model. In this method, each optimization round employs the first-order Taylor reduced order model to provide aerodynamic characteristics in the local design space around the baseline point. At the end of each optimization round, the baseline point moves toward the optima and a new reduced order model is built at the new baseline point for the next optimization round. In this way, the provided method explores the whole design space. The NACA0012 airfoils in subsonic and transonic flows are used to verify the method with the lift-drag ratio as optimization objective. The design parameters are the shape control parameters of the airfoil. The optimization algorithm is a genetic algorithm. After a total of 20 simulations by two rounds of optimizations, the lift-drag ratios increase from 0 to 25 and from 0 to 8 in the subsonic case and transonic case, respectively. An additional trick was suggested for addressing shockwave effect in the transonic case, in which the influence of the airfoil shape on the aerodynamic forces is divided into the following two parts: the smoothed part to address the influence of the shape on the smooth aerodynamic distribution, and the shockwave part to address the influence of the shape on shockwave strength, shockwave position, and their effect on the aerodynamic distribution. The optimizations of the airfoils in subsonic and transonic flows yield different trends. The results of the subsonic case tend to increase the airfoil curvature to increase the lift-drag ratio. The results of the transonic case tend to move the upper surface shockwave to the trailing edge, while moving the lower surface shockwave to the leading edge. Independent of the case, the provided optimization method can properly address the resulting trends and increase the efficiency of the optimization.

© 2020 Elsevier Masson SAS. All rights reserved.

1. Introduction

In recent years, multidisciplinary design optimization (MDO) [1, 2] and reliability analysis [3–6] of both aircrafts and aeroengines become increasingly important. However, these types of applications face two challenges: the large number of design variables and the computational time required by high-fidelity simulations (e.g., computational fluid dynamics (CFD) and finite element (FE)). The combination of these two challenges makes MDO and reliability analysis very time-consuming [7,8]. To overcome these problems, researchers have adopted design of experiments (DOE) [9], response surface [8], and sensitivity analysis [4,5,10] methods to alleviate the total computational burden. However, many costly simulations are still required. To further improve the efficiency

of MDO and reliability analysis, methods based on reduced order model (ROM) have been widely discussed.

ROM is a mathematical model for the prediction of the linear and weak-nonlinear dynamic characteristics of a wide class of systems at very low computational cost. It led to the development of several groups of methods, including proper orthogonal decomposition (POD) [9,11–13], harmonic balance (HB) [14–26], Volterra series [27–31], auto regression with exogenous input (ARX) [32–34], and neural networks [35]. Due to its high efficiency, ROM has been widely applied in research on aeroelastic analysis [36–38], flap control [39], wake excitation [23,27], flight dynamic estimation and control [40–42], and aerodynamic shape optimization [9–11]. An exhaustive summary of all relevant studies would exceed the scope of this paper. The following mainly discusses research about aerodynamic ROMs for optimization.

To address the optimization aspect, most studies focused on the POD ROM method for transonic problems with flow separations and shock waves. POD ROM is a linear combination of flow field snapshots. As a result, shock wave, flow separation and other non-

* Corresponding author.

E-mail address: lilizhou@163.com (L.Z. Li).

linearities that are presented in the snapshots can be obtained by POD prediction. LeGresley et al. [43] first discussed a POD method in airfoil inverse design problems, where the POD ROM was used to express the pressure field around a deformed airfoil. He suggested using unit cell Cartesian mesh as a common space for the storage of snapshots of deformed shapes. He also stated that the POD method cannot represent the entire solution space and will carry a certain error in prediction. Luo [44] suggested an optimization method based on nonlinear POD ROM to decrease flow separation at the end wall corners of a compressor. In his work, the flow field change due to compressor shape deviation was described by POD ROM, and additional response surfaces of weight coefficients were introduced into the POD ROM to consider nonlinear aerodynamic effects. Qiu et al. [7] applied POD for dimensionality reduction of design space and successfully decreased the total number of design variables while maintaining the generality of the original design space. Wu et al. [45] developed a benchmark aerodynamic shape optimization method based on POD. Interestingly, they used the POD method for shape parameterization instead of the commonly usage of expressing the relationship of flow field character due to shape deviation.

POD ROM is a linear combination of flow field snapshots, and any new added snapshot will introduce its flow feature into the ROM. This is a desirable behavior for the prediction of average physics characteristics; however, a POD approximation of this type would hide the physics characteristics behind the original snapshots [9]. To solve this problem, Iuliano et al. [9] suggested a zonal approach using a mixed full order model (FOM)/ROM. The FOM accurately solved the near wall boundary layer, non-linearity (e.g., shock wave) and flow separation where they occur. The ROM was applied to reconstruct the flow field far from the solid wall, where smoother and weakly varying solutions can be expected. Their zonal approach was reported to better solve the shockwave region and improve the prediction in transonic flow. Amsallem et al. [11] reported that the cost associated with the POD optimization procedure may scale with data dimensions. To reduce the dimensions, they suggested hyper-reduction method. For hyper-reduction method, most of the original large-scale computational domains were discarded and only a reduced portion of the state vectors of the domains were retained. This hyper-reduction method was combined with a radial basis surrogate model to optimize a nozzle model and a chemical reaction. LeGresley et al. [46] proposed a mesh reduction method based on a POD ROM coupled with a FOM solver. By comparing the POD results with a solution of known accuracy, the need and spatial extent for mesh reduction were determined. The results of transonic flow show that this method can generate good approximate solutions for flows of significant shock-wave movements.

Gradient optimization with POD has also been discussed. Two approaches were used to compute sensitivities (gradients) for the optimization: the direct method and the adjoint method [10,47]. In the direct method, sensitivity is directly computed, which requires solutions of POD or FOM for n_p times (n_p is the number of design parameters). The number of solutions is independent of the number of objectives and constraints. The adjoint approach calculated sensitivities by the differentiation of each objective function, which requires only two solutions of POD or FOM for one objective independent of the number of parameters involved. The direct method is preferable over the adjoint method when the number of objectives and constraints are larger than the number of parameters and vice versa. Zahr et al. [47] proposed an adaptive POD optimization approach, which uses POD as the substitute model providing flow character and which calculates the sensitivity via an adjoint method. Their approach uses a residual error indicator to maintain the optimization trajectory within a parameter space region of accurate ROM. If the ROM solution does not satisfy the

residual error indicator, the ROM is improved by more FOM samples. Li et al. [10] proposed a two-step optimization method which uses a gradient free algorithm combined with a kriging response surface to explore the whole design space and uses a following gradient-based optimization with POD for local optima. Both the adjoint formula for POD and FOM are derived to provide gradient information in this work.

This study provides a simple and efficient method for aerodynamic shape optimization based on a moving first-order-Taylor ROM. The proposed method divides the optimization process into several continual rounds. During an optimization round, the aerodynamic shape is optimized according to the data provided by the ROM. At the end of the optimization round, the baseline point of the ROM is moved to the previous optima and a new ROM is built. Then, a new optimization round is performed. Airfoils in subsonic and transonic flows are used to demonstrate the proposed method.

2. Aerodynamic optimization method based on the moving reduced order model

2.1. Hicks-Henne parameterization method

The Hicks-Henne method is used to parameterize the airfoil, in which a new airfoil is expressed as a linear combination of the baseline (initial) airfoil and Hicks-Henne bump functions [48,49]:

$$\begin{cases} y_u(x) = y_{u0}(x) + \sum_{i=1}^n f_i(x)a_i \\ y_d(x) = y_{d0}(x) + \sum_{i=1}^n f_i(x)b_i \end{cases} \quad (1)$$

where n represents the number of bump functions; x represents the coordinate in the chordwise direction; $y_u(x)$ and $y_d(x)$ represent the upper and lower surfaces of the new airfoil; y_{u0} and y_{d0} represent the upper and lower surfaces of the baseline airfoil; a_i and b_i represent the shape control parameters of the upper and lower surfaces, with a range from -0.01 to 0.01 as reported by Liao et al. [48]. $f_i(x)$ represents the Hicks-Henne shape bump functions:

$$f_i(x) = \begin{cases} x^{0.25}(1-x)e^{-20x}, & i = 1 \\ \sin^3(\pi x^{\log(0.5)/\log(x_i)}), & i \geq 2 \end{cases} \quad (2)$$

where x_i ($i = 1, 2, \dots, 6$) represents the coordinate of the i -th control knot and locates the maximum point of the bump function. In this paper, $x_1 = 0.15$, $x_2 = 0.3$, $x_3 = 0.45$, $x_4 = 0.6$, $x_5 = 0.75$ and $x_6 = 0.9$. This paper uses the Hicks-Henne method to parameterize the airfoil. However, different parameterization methods can also be used [48].

2.2. Aerodynamic reduced order model of the first order Taylor expansion

When an airfoil and its surrounding flow domain are considered as a system, the relationship between the airfoil shape and the aerodynamic forces can be expressed as:

$$\{p(x), \tau(x)\} = \Psi \{y_u(x), y_d(x)\} \quad (3)$$

where Ψ represents the aerodynamic system; $p(x)$ and $\tau(x)$ represent the airfoil pressure and the skin-friction coefficient, respectively.

Substituting Eq. (1) into Eq. (3) yields:

$$\{p(x), \tau(x)\} = \Psi \left\{ y_{u0}(x) + \sum_{i=1}^n f_i(x)a_i, y_{d0}(x) + \sum_{i=1}^n f_i(x)b_i \right\} \quad (4)$$

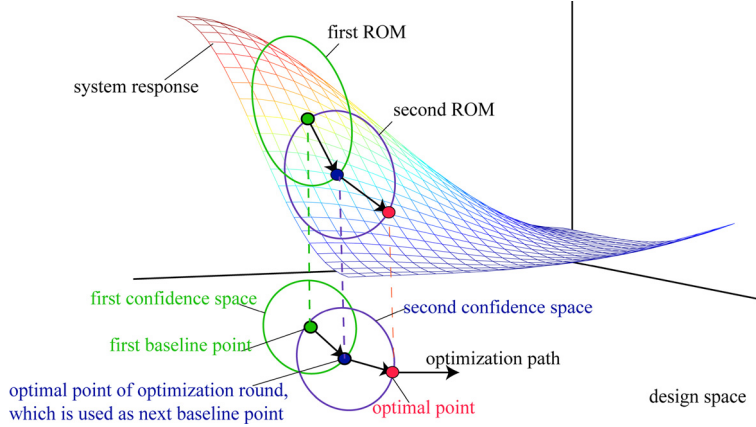


Fig. 1. Aerodynamic optimization based on the moving reduced order model.

As y_{u0} , y_{d0} , and f_i are already known, the system of Eq. (4) can be rewritten as:

$$\{p(x), \tau(x)\} = \Psi\{a_i, b_i\} \quad (5)$$

or

$$\{\mathbf{Y}\} = \Psi\{\mathbf{X}\} \quad (6a)$$

$$\mathbf{Y} = \{Y_i(x), i = 1, 2\} = \{p(x), \tau(x)\} \quad (6b)$$

$$\mathbf{X} = \{X_j, j = 1, 2, \dots, 12\} = \{a_i, b_i, j = 1, 2, \dots, 6\} \quad (6c)$$

This system can be expressed by the L -order Taylor expansion as:

$$\begin{aligned} \mathbf{Y}(x) &= \mathbf{h}_0(x) + \sum_{j_1=1}^m \mathbf{h}_1^{j_1}(x) X_{j_1} + \frac{1}{2} \sum_{j_1=1}^m \sum_{j_2=1}^m \left\{ \mathbf{h}_2^{j_1, j_2}(x) X_{j_1} X_{j_2} \right\} \\ &+ \frac{1}{6} \sum_{j_1=1}^m \sum_{j_2=1}^m \sum_{j_3=1}^m \left\{ \mathbf{h}_3^{j_1, j_2, j_3}(x) X_{j_1} X_{j_2} X_{j_3} \right\} + \dots \\ &+ \frac{1}{L!} \sum_{j_1=1}^m \dots \sum_{j_L=1}^m \left\{ \mathbf{h}_L^{j_1, \dots, j_L}(x) \prod_{f=1}^L X_{j_f} \right\} \end{aligned} \quad (7)$$

where \mathbf{Y} represents the output matrix; \mathbf{X} represents the input matrix; \mathbf{h}_0 represents the response matrix of baseline airfoil; $\mathbf{h}_L^{j_1, \dots, j_L}$ represents the L -order Jacobian term to input (the L -order response kernel).

In the Taylor expansion, the first-order Jacobian terms represent the linear influence, and they consist of n contributions. High order Jacobian terms indicate the nonlinear effects of the system. The second and third order Jacobian terms consist of $4n^2$ and $8n^3$ contributions. It is important to note that $\mathbf{h}_2^{j_1, j_2} = \mathbf{h}_2^{j_2, j_1}$. Thus, the Jacobian terms are symmetric with respect to the arguments, which reduces the total number of Jacobian terms to $2n^2 + n$. Similar properties hold for the third order Jacobian terms. The total number of the third order Jacobian terms may be reduced to $2/3(2n^3 + 3n^2 + n)$ [50]. In this paper, these Jacobians terms are identified by CFD simulation. Since input variables are numerous, identifying high order Jacobian terms is costly. Therefore, this paper uses first order Jacobian terms to predict aerodynamic forces. The first order Taylor ROM is of the form:

$$\begin{cases} p(x) = A_0(x) + \sum_{i=1}^n B_i(x)a_i + \sum_{k=1}^n C_k(x)b_i \\ \tau(x) = D_0(x) + \sum_{i=1}^n E_i(x)a_i + \sum_{i=1}^n F_i(x)b_i \end{cases} \quad (8)$$

where $A_0(x)$ represents the pressure coefficient of the baseline airfoil; $B_i(x)$ represents the kernel of the pressure coefficient corresponding to the i -th upper surface parameter a_i ; $C_i(x)$ represents the kernel of the pressure coefficient corresponding to the i -th lower surface parameter b_i ; $D_0(x)$ represents the skin friction coefficient of the baseline airfoil; $E_i(x)$ represents the kernel of the skin friction coefficient corresponding to the i -th upper surface parameter a_i ; $F_i(x)$ represents the kernel of the skin friction coefficient corresponding to the i -th lower surface parameter b_i . $A_0(x)$, $B_i(x)$, $C_i(x)$, $D_0(x)$, $E_i(x)$, and $F_i(x)$ are identified from CFD data.

The first order Taylor ROM is easy to be constructed. Its assumption is that the aerodynamic character changes can be expressed by linear superposition. This is only true if the shape change is small. In other words, the parameters must change in local space. However, one problem remains: the aerodynamic problem is globally nonlinear. Under this condition, the first order Taylor ROM cannot address the relationships between input and output of the whole design space. Optimization using this ROM is thus limited to a small local design space around a baseline point. To overcome this issue, a multi-round optimization method is proposed.

2.3. Multi-round optimization method based on the moving reduced order model

The multi-round optimization method divides the optimization process into several rounds (Fig. 1). During each round, optimization is performed using the first order Taylor ROM, which is specially built at the baseline point of this round. The search for optimization is limited to the local design space (the confidence space) in which the ROM can accurately represent the relationship between aerodynamic forces and design parameters.

The accuracy of the ROM and the optimization is assessed at the end of each round by comparing the aerodynamic forces of the ROM with those of CFD at the optimal point. The ROM confidence space is then adjusted accordingly. If the ROM is accurate, the confidence space can be expanded. The baseline point is moved to the optimal point and a new ROM is built at the new baseline point. Thus a new round of optimization is performed. If the ROM is not accurate, the confidence space is narrowed and optimized again. With the accumulation of data, the local ROMs will cover the optimization path and the whole design space is explored. In general, the method uses first order ROM to ensure optimization efficiency and uses moving ROM to address design space nonlinearity. It is important to note that the method uses first order Taylor ROM only for efficiency reasons. Any efficient and accurate linear and nonlinear ROM can be used for the method.

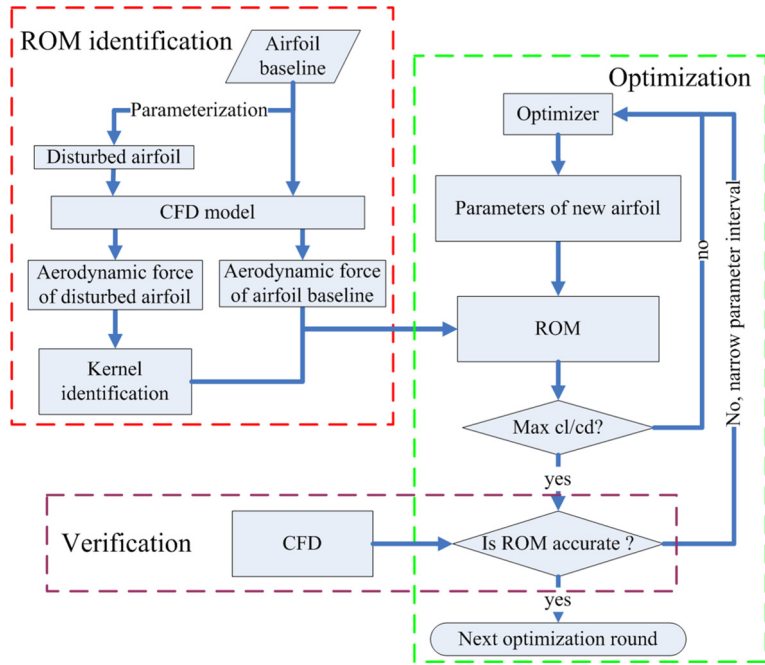


Fig. 2. Flow chart of optimization based on moving ROM.

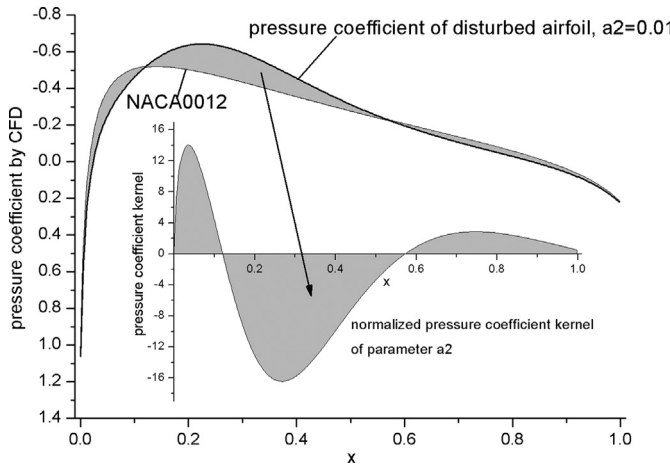


Fig. 3. Kernel calculation method.

The optimization process based on the moving ROM is divided into the following steps (Fig. 2):

- 1) Parameterize an airfoil to be optimized.
- 2) Calculate the aerodynamic forces of the baseline airfoil by CFD.
- 3) Disturb the airfoil parameters one by one; generate new meshes of the disturbed airfoils by mesh deformation or remesh method.
- 4) Calculate the aerodynamic forces of the disturbed airfoils by CFD.
- 5) Calculate the kernels of the aerodynamic forces corresponding to the shape design parameters.

Fig. 3 shows the kernel calculation method. The kernels in the ROM represent aerodynamic force increments induced by shape changes. These kernels are calculated by subtracting the aerodynamic forces of the baseline airfoil from those of disturbed airfoils. To normalize each kernel, the subtracted result is divided by the increment of shape parameter.

The subtraction is done at common nodes. When the CFD meshes are regenerated for the disturbed airfoils, they are inconsistent with the baseline airfoil mesh at the wall surfaces. Therefore, a common mesh is used to store and subtract aerodynamic forces following the method developed by LeGresley et al. [43]. In this paper, the common mesh is a sequence of nodes in chordwise arrangement. The aerodynamic data of the airfoil wall surfaces is interpolated into, stored at, and subtracted at these nodes.

- 6) Use the above kernels to build the ROM of aerodynamic forces by Eq. (8);
- 7) Optimize the airfoil to maximize its lift-drag ratio (Cl/Cd) which is calculated from the aerodynamic forces of the ROM;
- 8) Judge the ROM accuracy; adjust the confidence space.

The accuracy is judged by the error between the aerodynamic forces of the optimal airfoil calculated by ROM and those calculated by CFD. If the error is smaller than 5%, accept the optimal airfoil and extend the confidence space (e.g., the upper and lower limits of parameters are increased by 30% in this study) to accelerate the following optimization. If the error is between 5% and 15%, the optimal airfoil is accepted for this round. If the error exceeds 15%, abandon the optimal result, narrow the confidence space, and repeat Step 7) with the old ROM.

- 9) Move the baseline point to the optima, update ROM at the new baseline point, and perform the next round of optimization.
- 10) Repeat Steps 1) to 9) until the global optimum solution is found.

3. An example under subsonic condition

3.1. Modeling description

The optimization method is first validated by the NACA0012 airfoil in viscous subsonic flow at a free stream Mach number of 0.63 and an attack angle of 0° . Fig. 4 shows the domain and mesh for the establishment of ROM. The simulation uses a commercial solver. During the calculation, double precision, ideal-gas, and

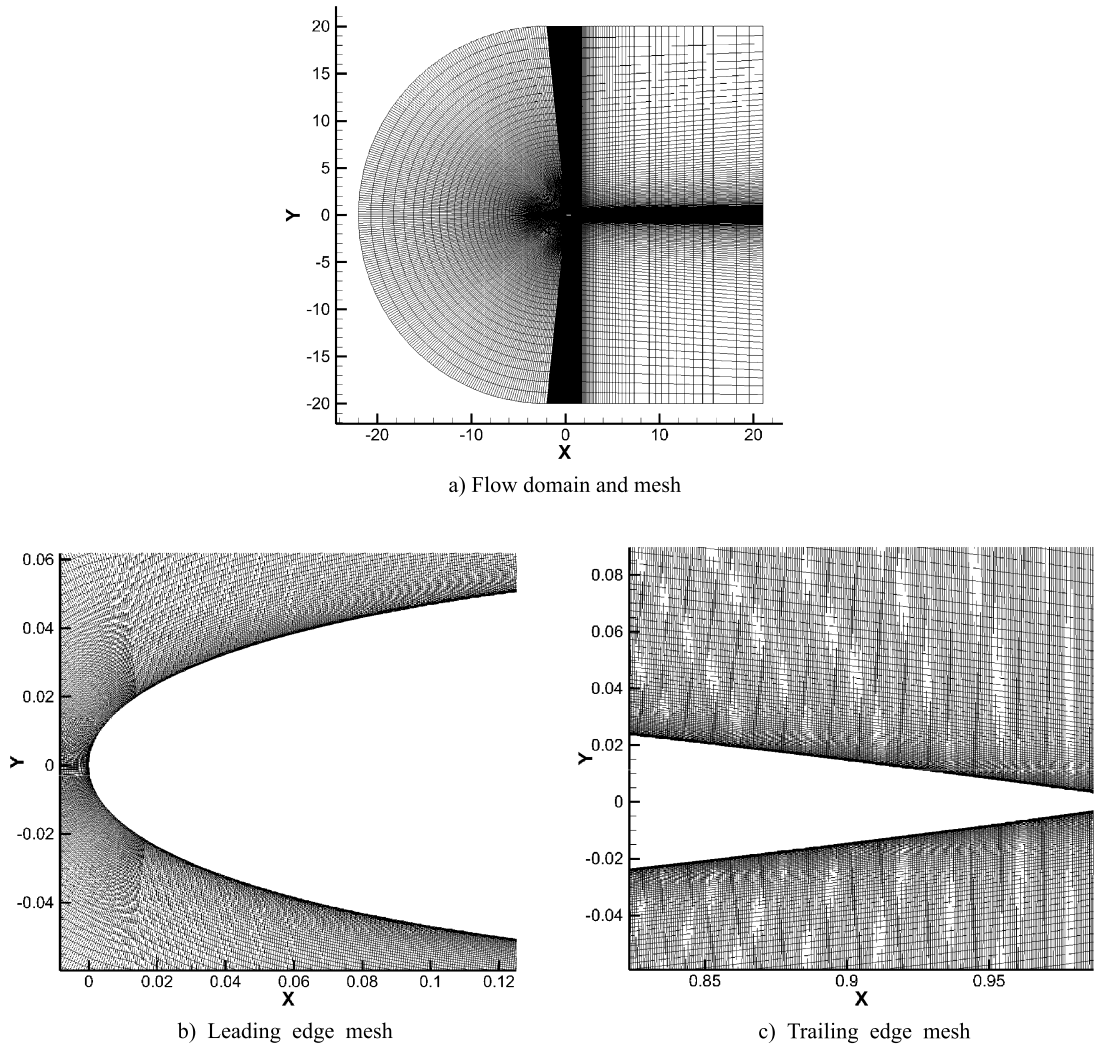


Fig. 4. Computational domain and mesh.

Spallart-Allmaras viscous model are applied. No slip wall is applied at the airfoil wall. The airfoil is parameterized by the Hicks-Henne method as described above. The design variables are the shape control parameters of the Hicks-Henne function. The optimization objective is to maximize the airfoil lift-drag ratio.

The CFD model is first verified at 0.63 Mach and an attack angle of 2° . The pressure coefficient calculated by the CFD model is compared with previously published data [48,49] (Fig. 5). The results show that the pressure coefficient by the CFD model agrees well with the experimentally obtained values, which indicates that the CFD model is credible. Therefore, this CFD model can be used to establish the ROM.

3.2. First round of optimization

Fig. 6 shows the first baseline airfoil (NACA0012) and the disturbed airfoils. All upper surface parameters are equal to 0.01. The aerodynamic coefficients (pressure and skin friction coefficients) of these airfoils are calculated by CFD at an attack angle of 0° and 0.63 Mach, as shown in Figs. 7 and 8. Following the method described in Section 2.3, the kernels of the aerodynamic coefficients are obtained (Figs. 9 and 10). These kernels are substituted into Eq. (8) to build the ROM. Then, the aerodynamic coefficients of different shape parameters can be predicted by the ROM.

The shape of NACA0012 airfoil is symmetric. The influence of the upper and lower surface parameters on the aerodynamic coef-

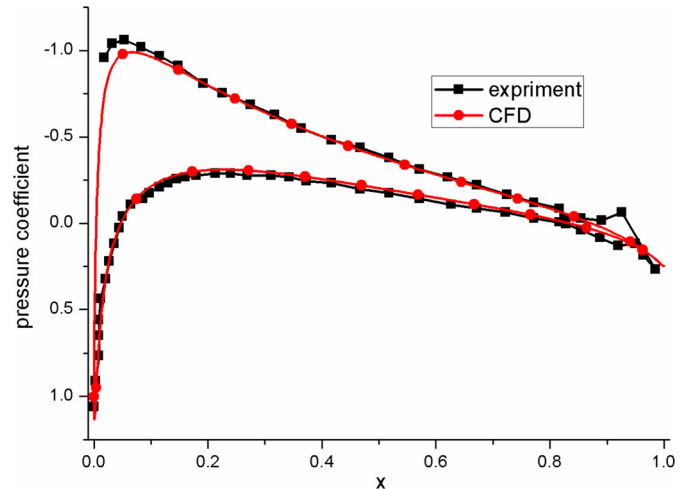


Fig. 5. Comparison of the test and CFD results in the subsonic case.

ficients is symmetric. Thus, Figs. 7 and 8 only show the pressure and skin friction coefficients due to the changes of the upper surface parameters. The kernels of the aerodynamic coefficients due to the lower surface parameters are the same as these due to the upper surface parameters. Therefore, only the kernels of the upper surface are shown in Figs. 9 and 10.

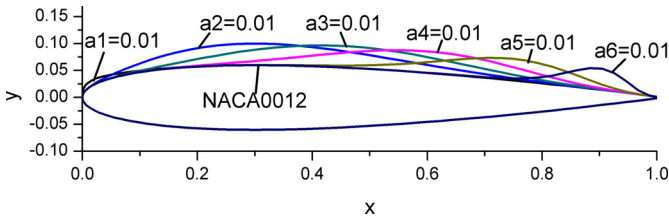
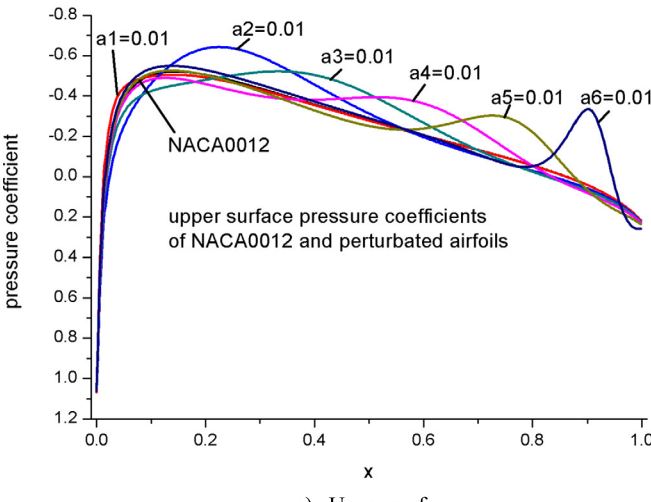


Fig. 6. Shapes of the baseline and disturbed airfoils.

Comparison of the aerodynamic forces of the upper and lower surfaces (Figs. 7 and 8) indicates that the changes of the upper surface shape at this level exert little impact on the lower surface aerodynamic forces. To simplify the ROM, the upper and lower surfaces are assumed to be independent. Consequently, the upper surface parameters only affect the upper surface aerodynamic forces, while the lower surface parameters only affect the lower surface aerodynamic forces. Figs. 7 to 10 also indicate that the influence intensity and range of parameter a_1 are the smallest, while those of parameter a_6 are the largest.

Then, we substitute the kernels shown in Figs. 9 and 10 into Eq. (8) to build the local ROM for the NACA0012 airfoil. The variation range (confidence space) of all design parameters for the ROM

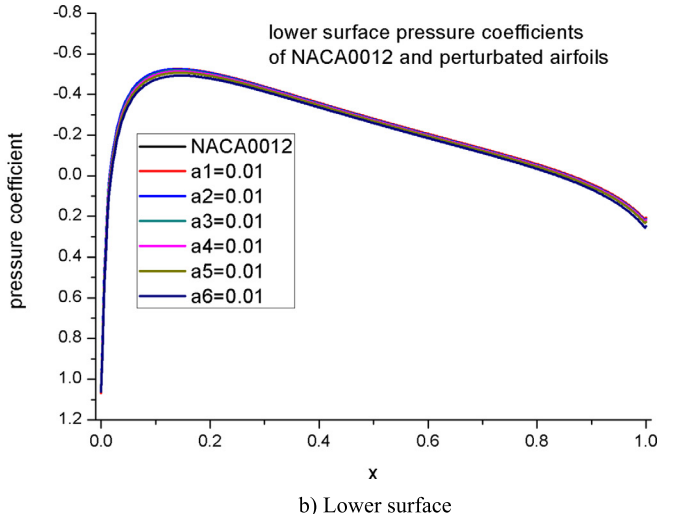


a) Upper surface

is $[-0.01, 0.01]$. This ROM's accuracy is verified in Section 3.4. The lift-drag ratio (C_l/C_d) is defined as the optimization objective.

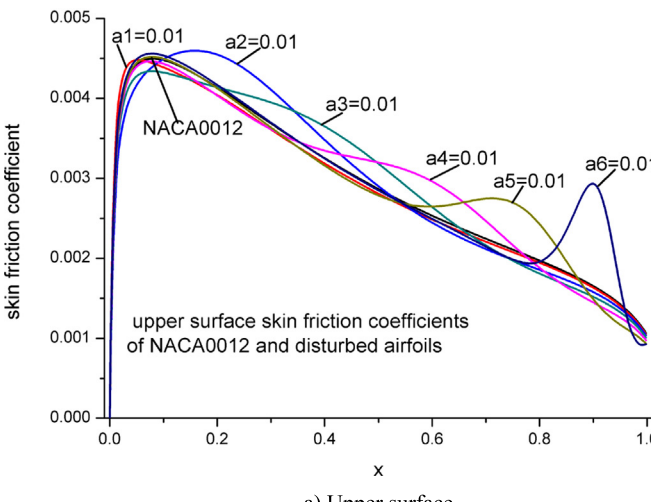
The first round of optimization uses a genetic algorithm (GA). Traditionally, optimization algorithms can be divided into two broad categories [10]: gradient-based methods and gradient free methods. The gradient-based method requires gradient information of the objective function to guide the optimization process (e.g., the quasi-Newton method). The main advantage of this type of method is its rapid convergence, especially if the gradient is obtained with the adjoint method. The gradient free method is typically based on surrogate models and evolutionary algorithms (e.g., GA together with the kriging response surface). This type of method is robust, compatible and slow. In addition to its ease of implementation, the method is suitable for nonlinear optimization problems with multiple local optima. Practically, two-step optimization method is used. The gradient free method identifies several local optima slowly in the first step. The gradient-based method rapidly identifies the exact global optima [10], using these local optima as initial values in the second step. This paper uses only a gradient free method, GA. This may result in time wasting during the final convergence, but no possible global optima would be missed out.

During the optimization, the lift-drag ratio is found to oscillate between positive and negative large value. Analysis indicates

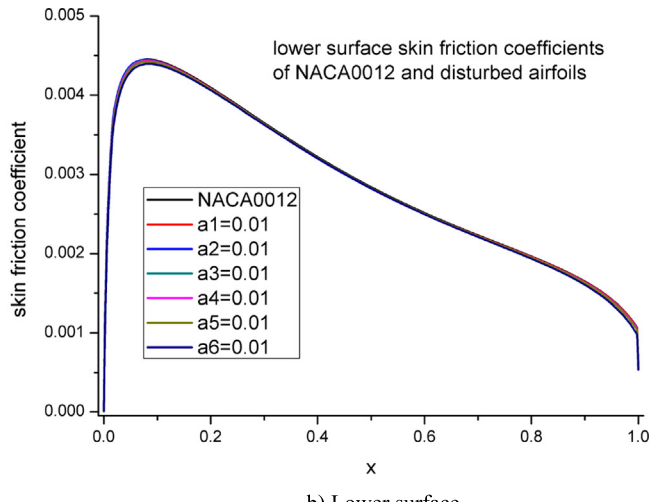


b) Lower surface

Fig. 7. Pressure coefficients of the baseline and disturbed airfoils for the subsonic case.



a) Upper surface



b) Lower surface

Fig. 8. Skin friction coefficients of the baseline and disturbed airfoils for the subsonic case.

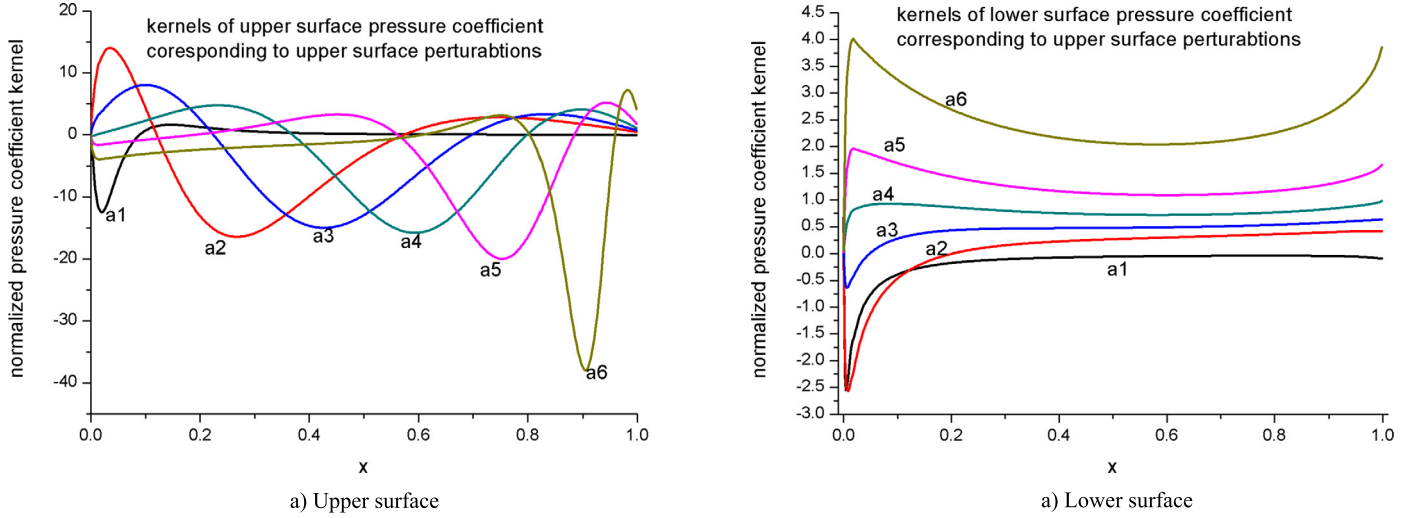


Fig. 9. Kernels of pressure coefficient in the subsonic case.

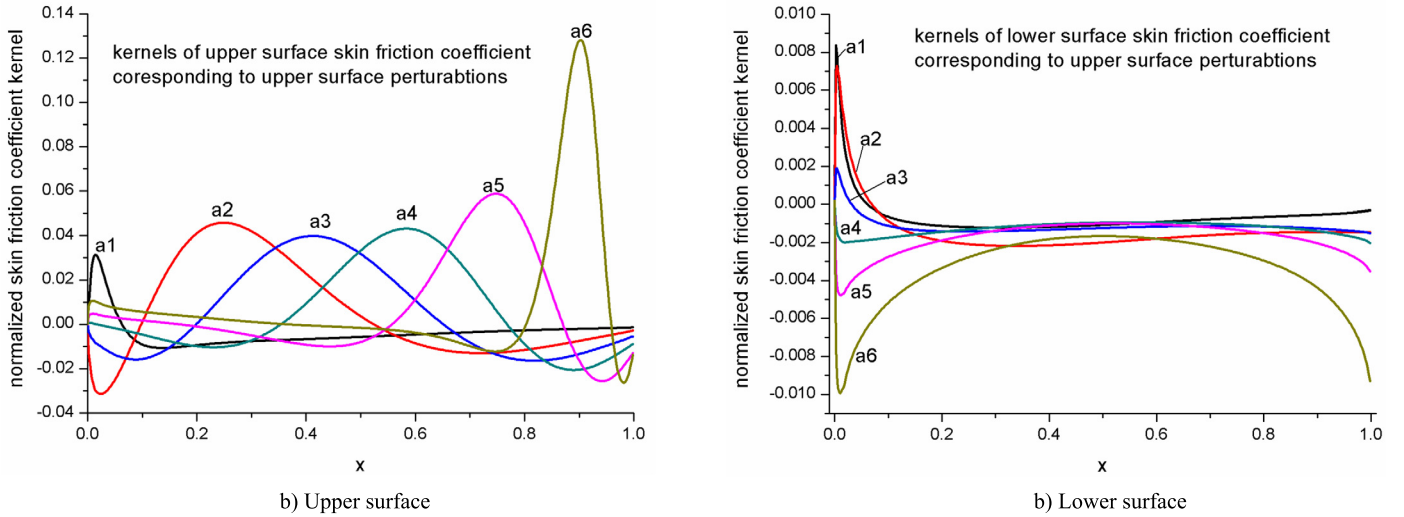


Fig. 10. Kernels of skin friction coefficient in the subsonic case.

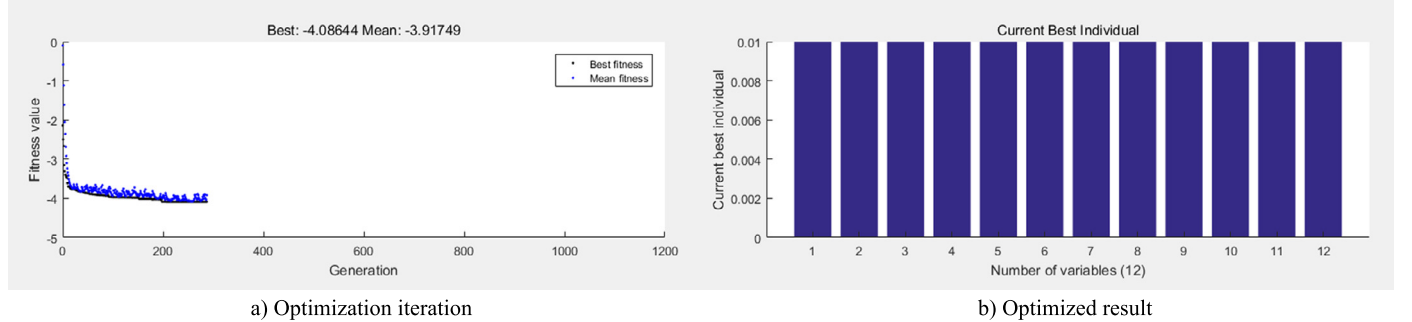


Fig. 11. First round iteration in the subsonic case.

that the denominator of the lift-drag ratio, i.e. the drag coefficient (C_d), is close to zero. Due to the error of the ROM, the drag value jumps between small positive and negative values. The lift-drag ratio jumped between large positive and negative values as a result. Therefore the lift-drag ratio can not be used as the optimization objective to assess the aerodynamic character of airfoils. After several trials, the objective is set to $C_l / (0.05 + C_d)$ to suppress the jump of the objective value.

Then, the airfoil is optimized by the ROM. The total iteration number of the first optimization round is 326 (Fig. 11). The optimal airfoil is shown in Fig. 12a and the optimal pressure and friction coefficients are shown in Figs. 12b and 12c. The optimal parameters and lift-drag ratio are listed in Table 1. The optimal lift-drag ratio is 17.826 as calculated by ROM.

The aerodynamic forces of the optimal airfoil are also analyzed by CFD. The optimal lift-drag ratio is 19.449 as calculated by CFD

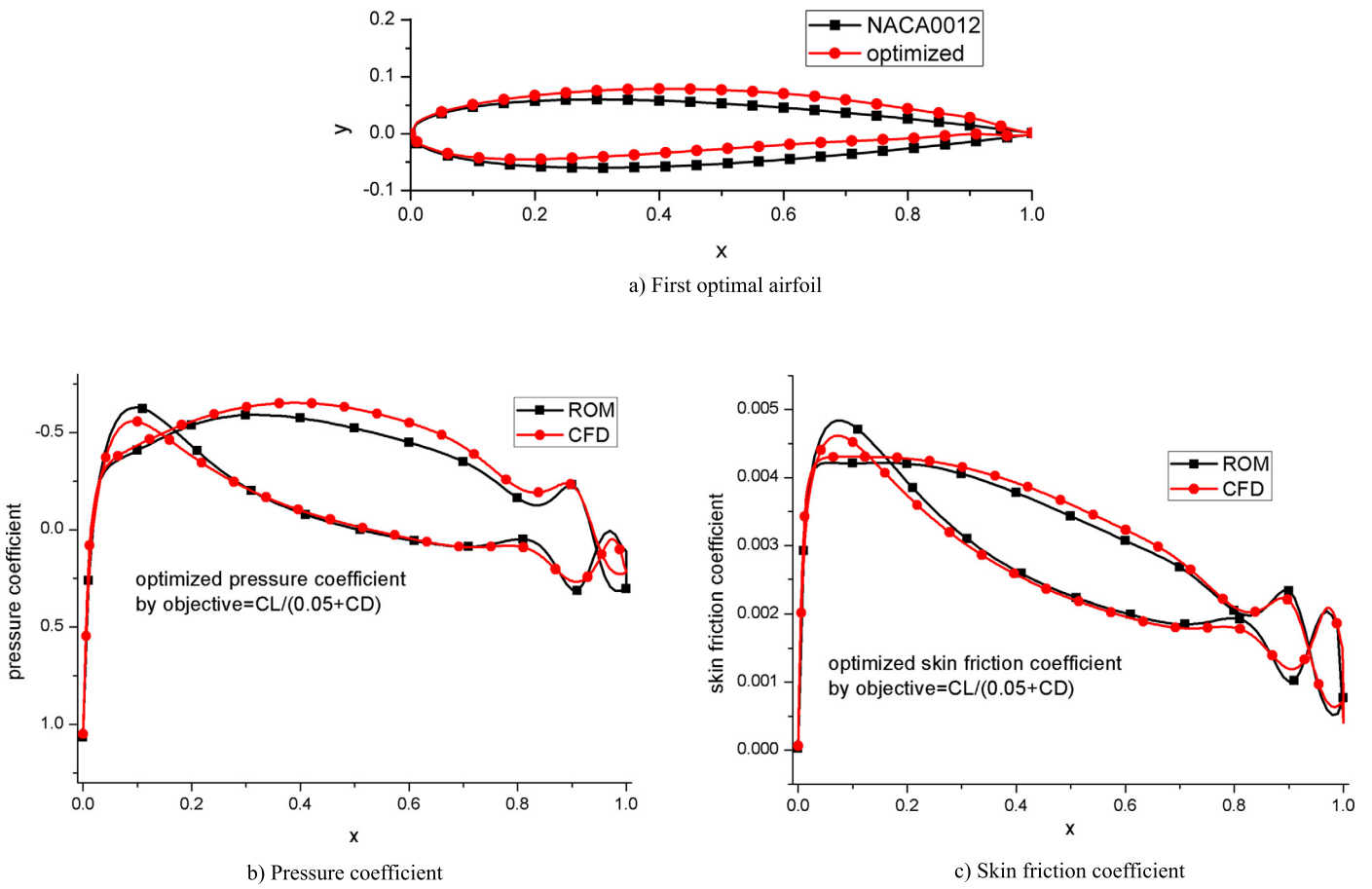


Fig. 12. Optimal results of the first round for the subsonic case.

Table 1
First round optima for the subsonic case.

Optimal parameters						
Upper surface	a1 0.01	a2 0.0065	a3 0.01	a4 0.01	a5 0.01	a6 0.01
Lower surface	b1 0.01	b2 0.01	b3 0.01	b4 0.01	b5 0.01	b6 0.01
Optimal lift/drag ratio	by ROM 17.826		by CFD 19.449			

(Table 1). The error is 8.3% which remains below 15%. Figs. 12b and 12c compare the ROM and CFD aerodynamic forces of the optimal airfoil. The result indicates that the ROM results are acceptable. Therefore, the ROM can be used for the optimization and the optimization method based on the ROM is feasible.

This first optimization round uses about 4 h of computational time, which include: the CFD analysis time for the baseline airfoil (0.5 h, one simulation), the CFD analyses time for the six kernels (0.5 h each, six simulations), and the time of optimization iteration (12 min for 326 iterations, no simulation). If CFD were used in all 326 iterations, the total optimization time would be 163 h. Therefore, it can be concluded that the optimization efficiency is greatly improved by the ROM.

3.3. Second round optimization by moving reduced order model

The first-round optimal airfoil is used as the new baseline during the second round. And then the ROM is updated by the same method in the first round. The second group of kernels is shown in Figs. 13 and 14. In the figures, the line markers are the parame-

Table 2
Second round optima for the subsonic case.

Optimal parameters						
Upper surface	a1 0.01	a2 0.01	a3 0.01	a4 0.01	a5 0.01	a6 0.01
Lower surface	b1 0.01	b2 0.01	b3 0.01	b4 0.01	b5 0.01	b6 0.01
Optimal lift/drag ratio	by ROM 25.3575		by CFD 25.3941			

ter names corresponding to the kernels. By substituting the kernels into Eq. (8), the second ROM is obtained.

In the second round, the parameter confidence ranges are $[-0.01, 0.01]$ unadjusted. The total iteration number is 120 (Fig. 15). The optimal design parameters and lift-drag ratio are shown in Table 2. The optimal lift-drag ratio calculated by ROM is 25.358. The optimal airfoil is shown in Fig. 16a. The aerodynamic forces of the optimal airfoil are also calculated by CFD. The optimal lift-drag ratio calculated by CFD is 25.394. This is identical to the ratio calculated by ROM. Figs. 16b and 16c compare the ROM and CFD aerodynamic forces of the optimal airfoil. The results indicate that they are identical.

The total time of this optimization round is ~ 7 h for 13 simulations, which includes: the CFD analysis time of the baseline airfoil (0.5 h, one simulation), the CFD analysis time of 12 kernels (0.5 h each, 12 simulations), and the time of the optimization iteration (12 min for 120 iterations, no simulation). If all 120 iterations used CFD, the total optimization time would be 60 h.

By two round optimizations, the lift-drag ratio increases to 25.3. Since this optimization is only a test example, it stops here. If a

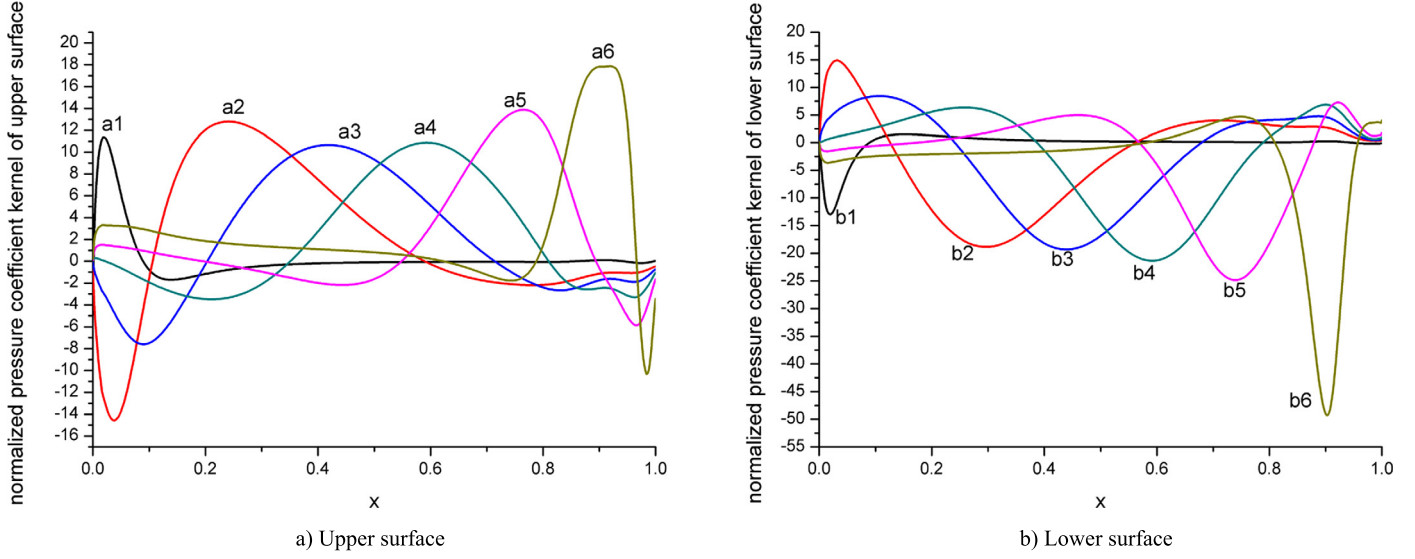


Fig. 13. Second group of kernels of the pressure coefficient for the subsonic case.

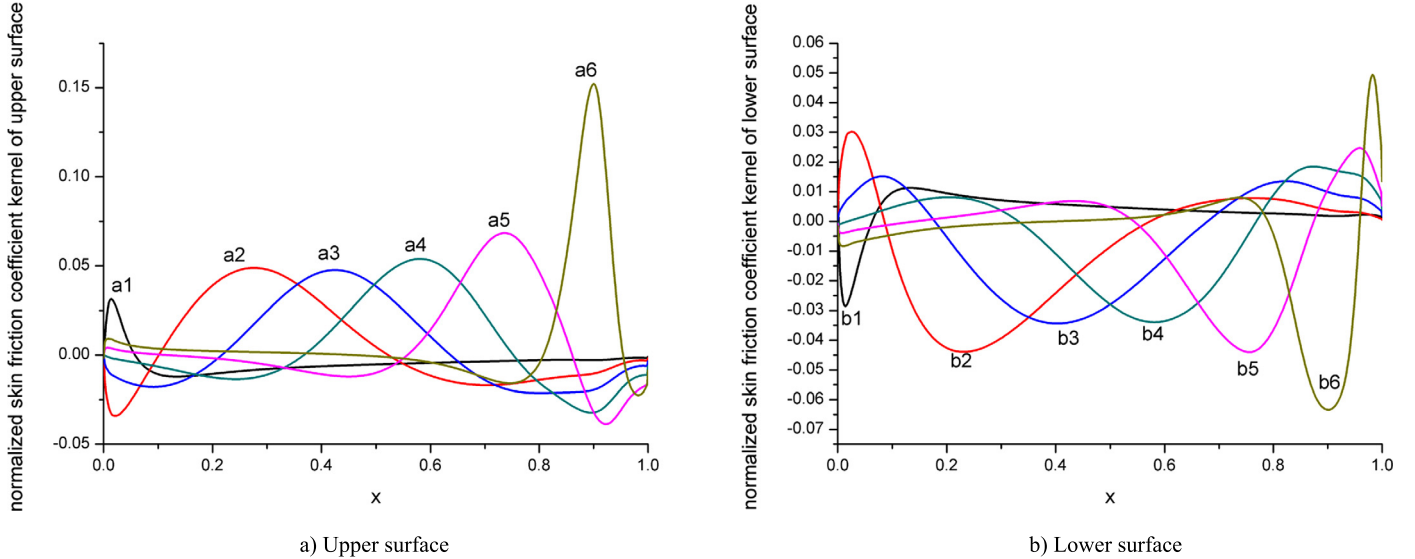


Fig. 14. Second group of kernels of the skin friction coefficient for the subsonic case.

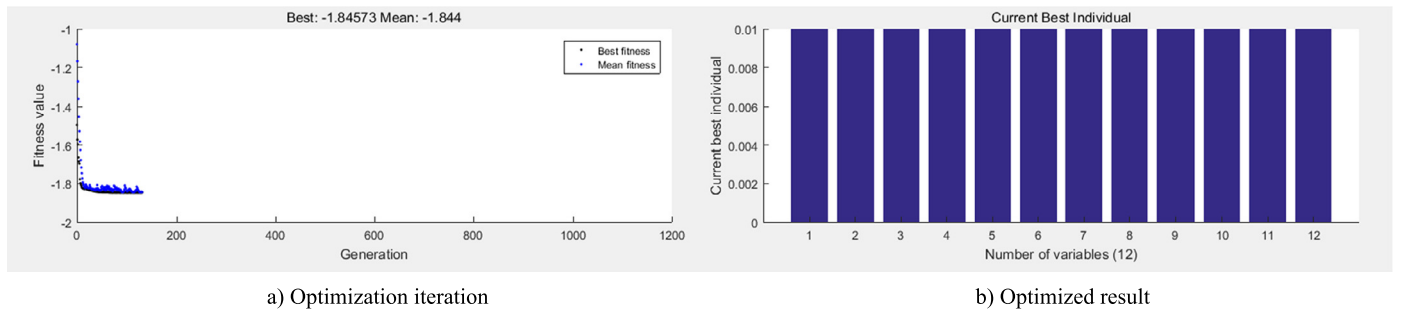


Fig. 15. Second round iteration for the subsonic case.

higher lift-drag ratio is required, further optimization can be initiated.

3.4. ROM error discussion

This section discusses the impact of the confidential space on the ROM error. The NACA0012 airfoil is used as the baseline air-

foil and the following four confidential spaces are investigated: $[-0.005, 0.005]$, $[-0.01, 0.01]$, $[-0.02, 0.02]$ and $[-0.03, 0.03]$. Figs. 17 and 18 compare the upper surface pressure and skin friction coefficients of the airfoils as calculated by CFD and ROM, where all parameters are set to their maximum possible values. Fig. 19 shows the ROM errors. The ROM errors are estimated by

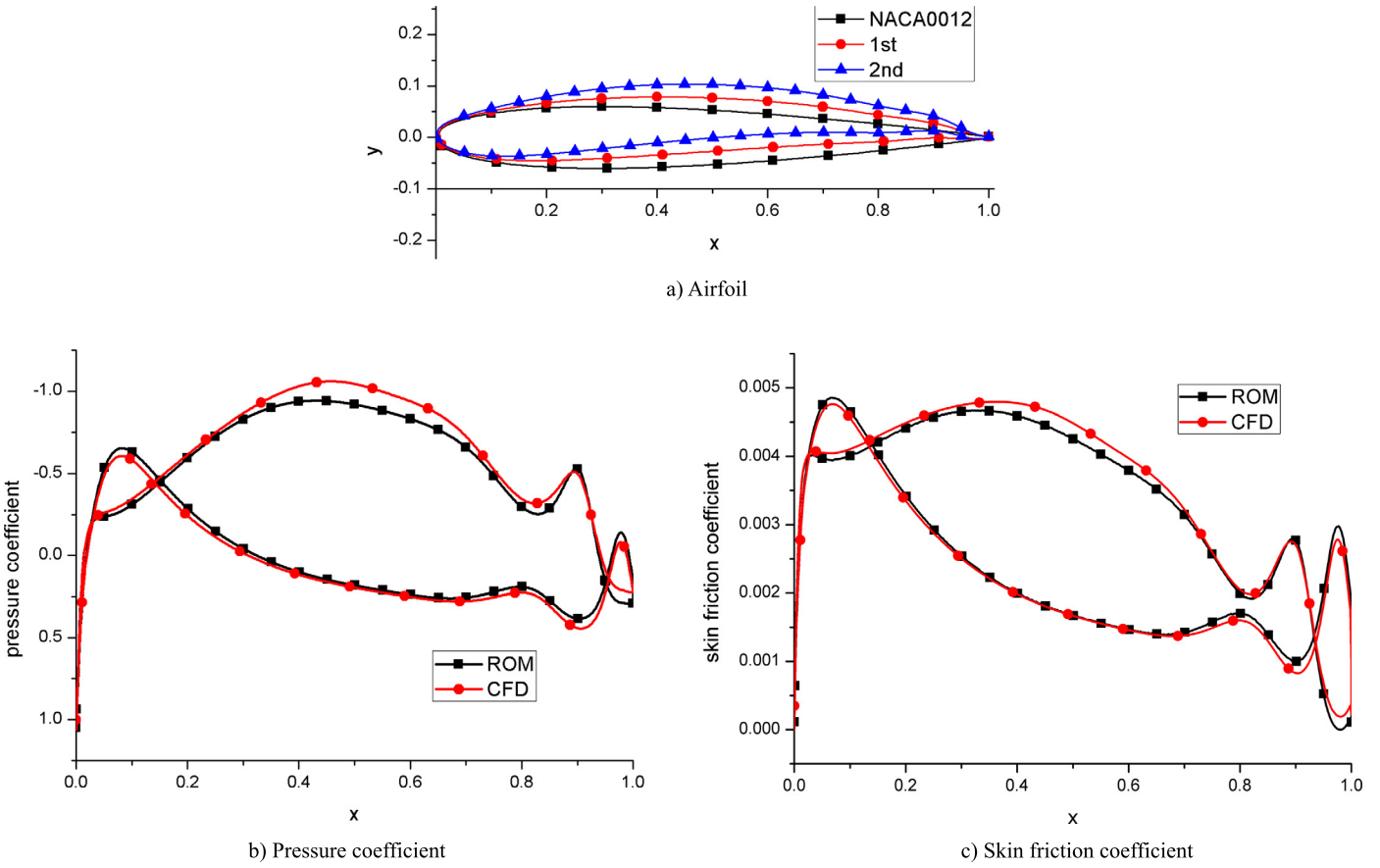


Fig. 16. Second round optima for the subsonic case.

the difference between the aerodynamic forces calculated by CFD and those calculated by ROM.

It can be found that the ROM and CFD results are identical when the parameters are below 0.01. The error is larger when the parameter values are between 0.01 and 0.02, but the ROM can still reflect the characteristics of the system. The error is excessively large when the parameter values exceed 0.02, and the ROM cannot represent the system characteristics. In general, ROM generates a small error when the parameter values are small. When the parameter values are large, non-linear characteristics will emerge and the ROM results will depart from the system characteristics.

The errors of the aerodynamic forces are small at the profile center and the leading edge, and are large at the trailing edge. The airfoil shape and its aerodynamic forces of the trailing edge are mainly controlled by parameters a_6 and b_6 . Figs. 9, 10, 13, and 14 show that the influence of a_6 and b_6 on the aerodynamic forces is much larger than the influence of other parameters. A large value of parameter a_6 (or b_6) may cause flow separation at the trailing edge, which may lead to a deviation of the aerodynamic system from its small disturbance state (Fig. 20d). Under this condition, the non-linearity of the system is significant, which leads to inconsistency of the ROM and CFD results. Therefore, the ROM is more suitable for a small disturbance problem. The moving ROM optimization method is the best choice for this condition.

4. An example under transonic condition

4.1. Modeling description

The moving ROM optimization method is validated by the NACA0012 airfoil at 0.85 Mach, an attack angle of 0° and inviscid [51]. The optimization method, mesh, solver, and wall bound-

ary condition are identical to those of the subsonic case. The CFD model is first verified. The pressure calculated by CFD is compared with previously published data [51] (Fig. 21), which shows that the simulation results agree with the reference. This indicates that the CFD model is credible and therefore, the CFD model can be used to establish the ROM.

4.2. Problem raised in the transonic case and its solution

Following the steps described in Sections 2 and 3 to establish a ROM for the transonic case, the pressure coefficients of both the baseline (NACA0012) and the disturbed airfoils are calculated by CFD at 0.85 Mach and an attack angle of 0° (Fig. 22). The kernels of the pressure coefficients due to the parameter changes are obtained (Fig. 23). The NACA0012 airfoil is symmetric. Thus, the figures only show the pressure coefficients that disturb the upper surface parameters. We build the transonic ROM by substituting the kernels into Eq. (8). Then, the pressures of any similar airfoil can be predicted by the ROM.

Pressure coefficients of two new airfoils are predicted by the ROM. One airfoil is $a_1 = a_2 = a_3 = a_4 = a_5 = a_6 = 0.005$ and $b_1 = b_2 = b_3 = b_4 = b_5 = b_6 = 0$. The other airfoil is $a_1 = a_2 = a_3 = a_4 = 0.005$, $a_5 = 0.002$, $a_6 = 0.001$, and $b_1 = b_2 = b_3 = b_4 = b_5 = b_6 = 0$. Fig. 24 shows the upper surface pressure coefficients of both airfoils calculated by ROM and CFD. The figure indicates that the ROM is not accurate. The ROM pressure matches the CFD result well before the shockwave ($x < 0.7$), but the pressures are completely different in the shockwave range $x \in 0.7-1.0$. Decreasing parameter values cannot increase the accuracy of the ROM (Fig. 24b).

The airfoil shape mainly affects the shockwave position of the airfoil in transonic flow. This cannot be addressed by the ROM of

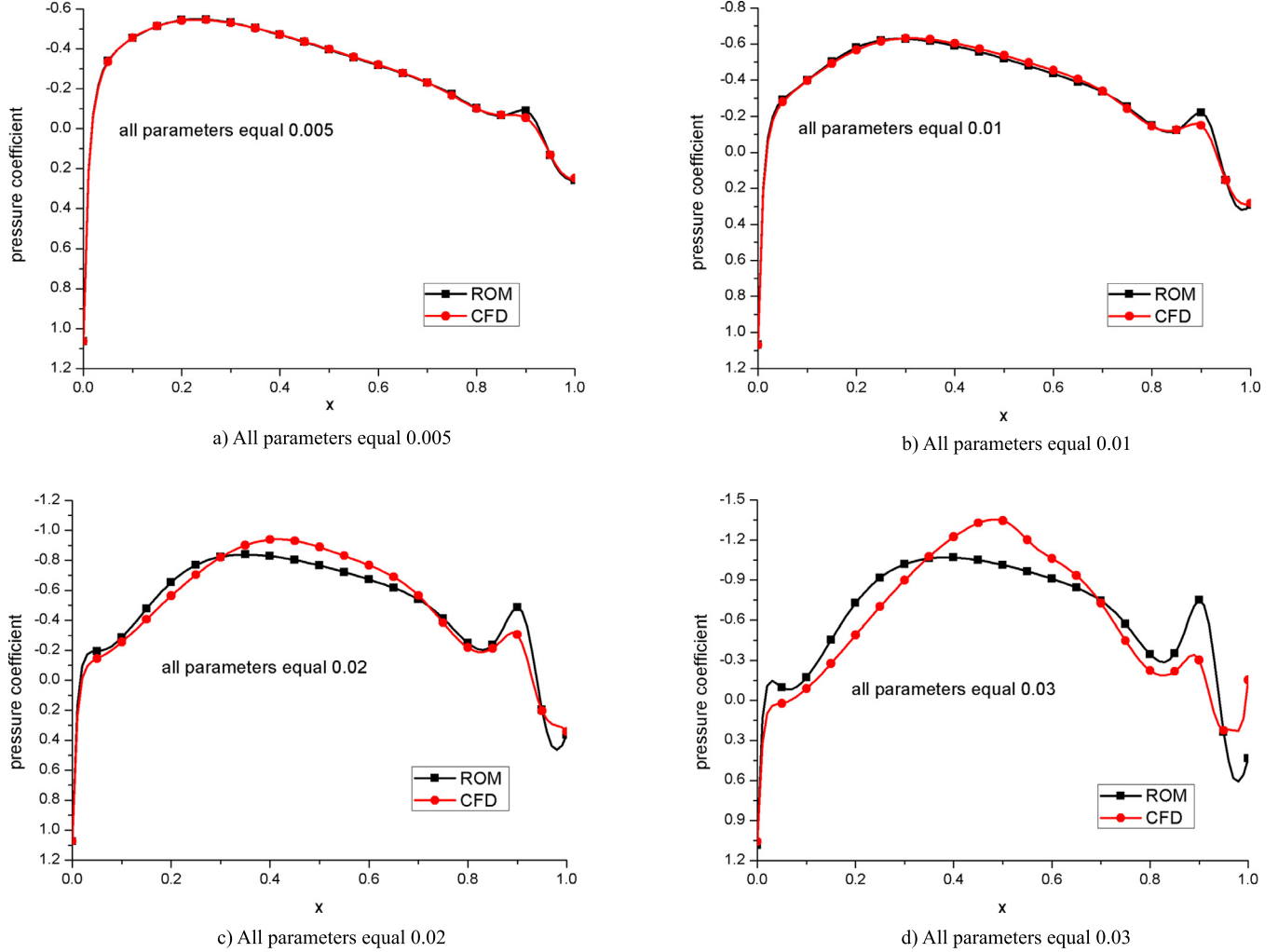


Fig. 17. Pressure coefficients of different parameter values for the subsonic case.

Section 3. Therefore, a ROM considering shockwave is developed for the transonic condition. The ROM is still based on the idea of the Taylor ROM. The aerodynamic force variation due to shape perturbations in the ROM is divided into two parts: the smoothed part and the shockwave part.

The smoothed part represents the smooth change of the aerodynamic forces due to shape deviation and is directly expressed by the Taylor ROM of Section 3. The word ‘smoothed’ used here describes the elimination of the sudden change of aerodynamic forces which is induced by the shockwave. The elimination is achieved by artificially adding the shockwave pressure increment to the pressure behind the shockwave and by smoothing the burrs of the aerodynamic force distribution.

The shockwave part represents the sudden change of aerodynamic forces due to the shockwave. The shockwave part is expressed by both the shockwave strength (pressure increment) and the shockwave position, which are expressed by two additional Taylor series terms here. The final ROM for the transonic problem is:

$$\begin{cases} p(x) = A_{sm,0}(x) + \sum_{i=1}^n B_{sm,i}(x)a_i + \sum_{k=1}^n C_{sm,k}(x)b_i + \Delta p_{sk}(x) \\ \tau(x) = D_{sm,0}(x) + \sum_{i=1}^n E_{sm,i}(x)a_i + \sum_{i=1}^n F_{sm,i}(x)b_i + \Delta \tau_{sk}(x) \end{cases} \quad (9a)$$

$$\begin{cases} \Delta p_{sk} = \begin{cases} 0, & x < x_{sk} \\ \Delta p_{sk,0} + \sum_{i=1}^n B_{sk,i}(x)a_i + \sum_{k=1}^n C_{sk,k}(x)b_i, & x \geq x_{sk} \end{cases} \\ \Delta \tau_{sk} = \begin{cases} 0, & x < x_{sk} \\ \Delta \tau_{sk,0} + \sum_{i=1}^n E_{sk,i}(x)a_i + \sum_{k=1}^n F_{sk,k}(x)b_i, & x \geq x_{sk} \end{cases} \end{cases} \quad (9b)$$

$$x_{sk} = x_{sk,0} + \sum_{i=1}^n B_{xsk,i}(x)a_i + \sum_{k=1}^n C_{xsk,k}(x)b_i \quad (9c)$$

where $A_{sm,0}$ represents the smoothed pressure of the baseline airfoil; $B_{sm,i}$ represents the kernel of the smoothed pressure due to the change of the parameter a_i ; $C_{sm,k}$ represents the kernel of the smoothed pressure due to the change of the parameter b_i ; $D_{sm,0}$ represents the smoothed skin friction of the baseline; $E_{sm,i}$ represents the kernel of the smoothed skin friction due to the parameter a_i ; $F_{sm,i}$ represents the kernel of the smoothed skin friction due to the parameter b_i ; Δp_{sk} represents the pressure increment due to shockwave; $\Delta p_{sk,0}$ represents the shockwave pressure increment of the baseline; $B_{sk,i}$ represents the kernel of the shockwave pressure increment due to the parameter a_i ; $C_{sk,k}$ represents the kernel of the shockwave pressure increment due to the parameter b_i ; $\Delta \tau_{sk}$ represents the shockwave skin friction increment due to the shockwave; $\Delta \tau_{sk,0}$ represents the shockwave skin friction increment due to the shockwave.

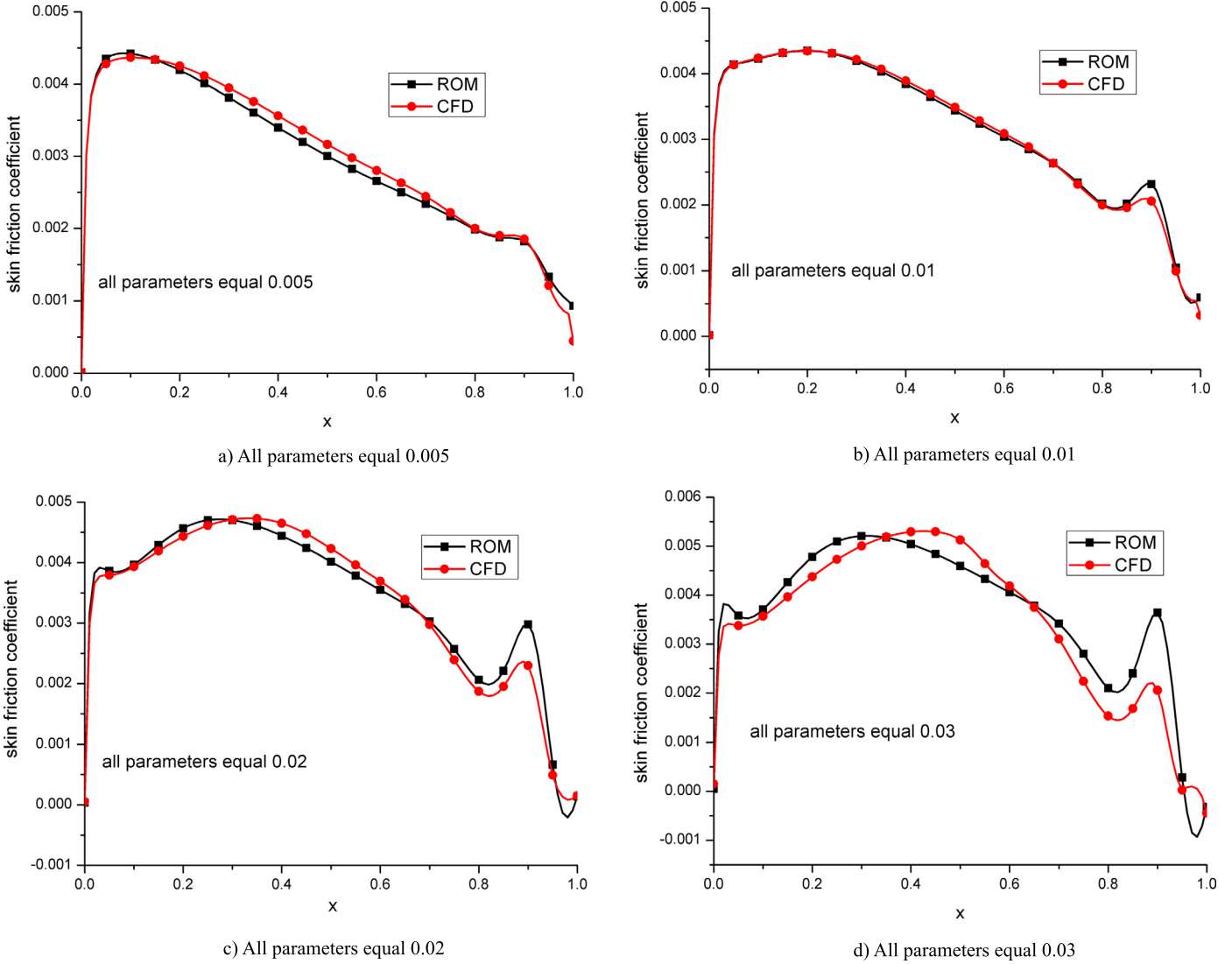


Fig. 18. Skin friction coefficients of different parameter values for the subsonic case.

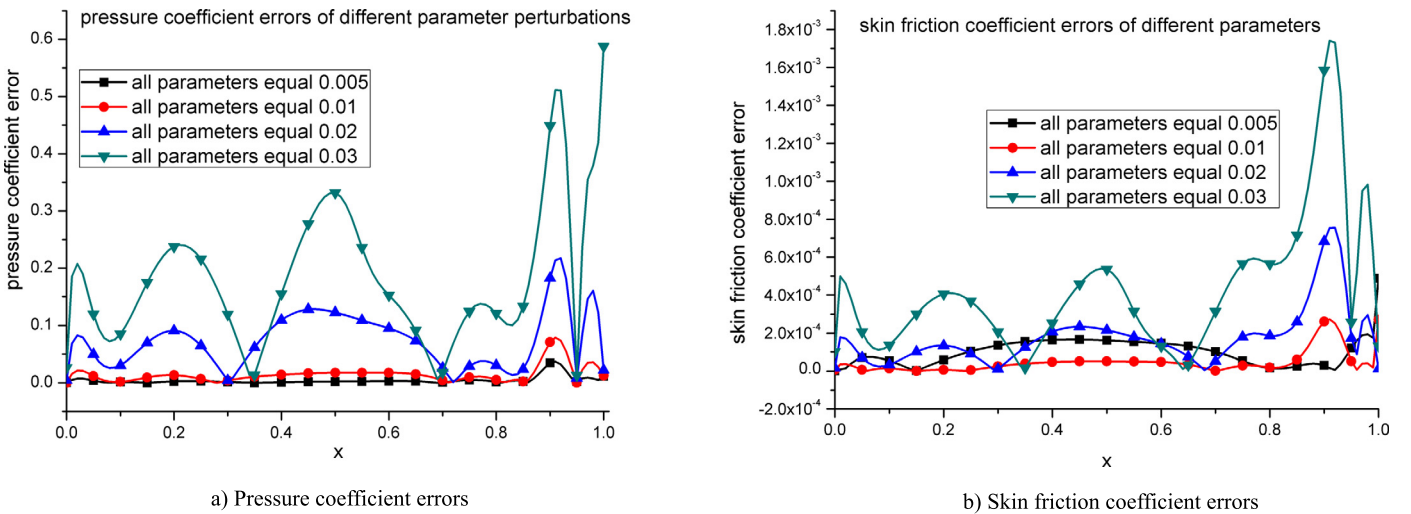


Fig. 19. Aerodynamic force errors of different parameter values for the subsonic case.

tion increment of the baseline; $E_{sk,i}$ represents the kernel of the shockwave skin friction increment due to the parameter a_i ; $F_{sk,k}$ represents the kernel of the shockwave skin friction increment due

to the parameter b_i ; x_{sk} represents the shockwave position; $x_{sk,0}$ represents the shockwave position of the baseline; $B_{xsk,i}$ represents the kernel of the shockwave position due to the parameter

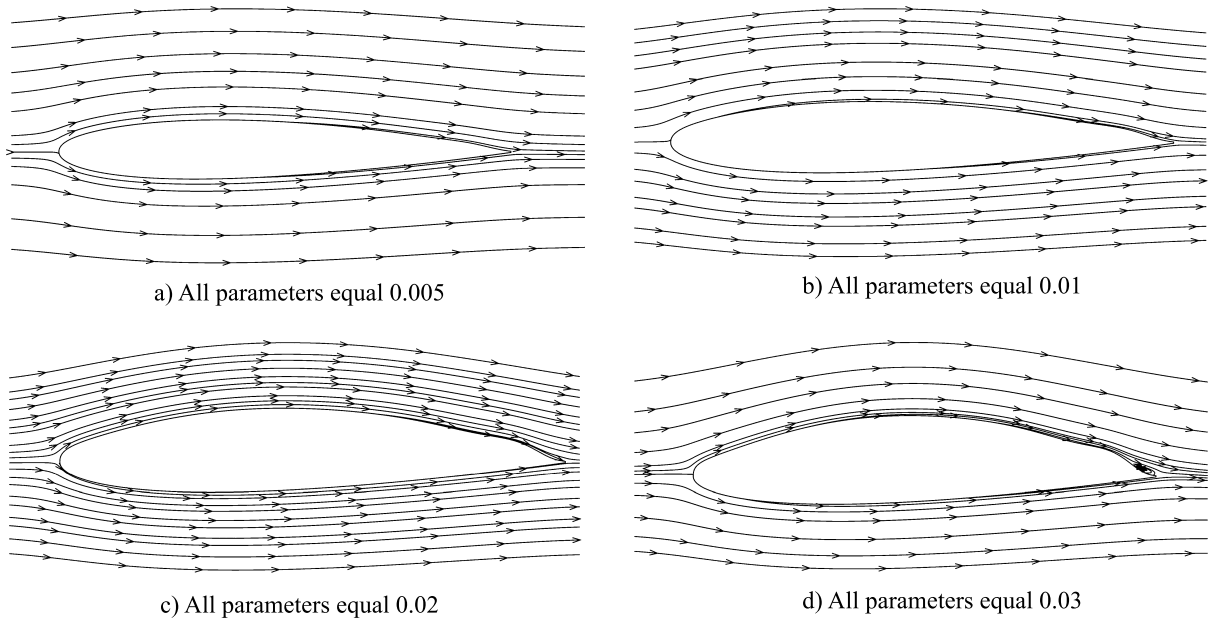


Fig. 20. Streamlines of different parameter values for the subsonic case.

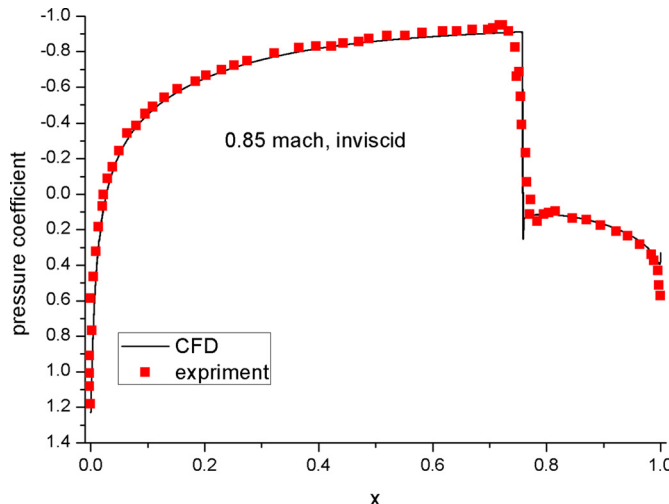


Fig. 21. Verification of the CFD model in the transonic case.

Table 3
Shockwave pressure increment and shockwave position of the baseline.

Pressure coefficient increment $\Delta p_{sk,0}$	Upper surface	1.04
	Lower surface	1.04
Shockwave position $x_{sk,0}$	Upper surface	0.759
	Lower surface	0.759

a_i ; $C_{xsk,k}$ represents the kernel of the shockwave position due to the parameter b_i .

A ROM is built from the data of Fig. 22. The smoothed pressure coefficient is shown in Fig. 25. The kernels of the smoothed pressure coefficient corresponding to the upper surface parameters, are shown in Fig. 26. The shockwave pressure coefficient increments and shockwave position of the baseline airfoil are listed in Table 3. The kernels of the shockwave pressure increments and shockwave position changes due to the upper surface parameter changes are listed in Table 4. Since the airfoil is symmetric, only the kernel data corresponding to the upper surface parameters are shown here.

The data of Figs. 25–26 and Tables 3–4 are substituted into the ROM with the consideration of shockwave (Eq. (9)). The pressure coefficients of the both airfoils shown in Fig. 24 are predicted by ROM again (Fig. 27). For comparison, Fig. 27 shows the pressure coefficients calculated by CFD (annotated by 'CFD'), by the ROM considering shockwave (annotated by 'Shock') and by the ROM without considering shockwave (annotated by 'ROM'). The figure indicates that the ROM considering shockwave can address the pressure increment induced by the shockwave. Moreover, the accuracy of the ROM can be increased by limiting the ranges of the design parameters a_5 and a_6 .

4.3. First optimization round of the transonic case

Using the ROM described in Section 4.2, the airfoil is optimized for the first round. The confidence ranges of the design parameters are $[-0.005, 0.005]$ for a_1 - a_4 and b_1 - b_4 , $[-0.002, 0.002]$ for a_5

Table 4
Kernels of shockwave pressure increment and shockwave position change due to upper surface parameter changes.

Shape control parameter	Kernel of surface pressure coefficients increment $B_{sk,i}$		Kernel of upper surface shockwave position $B_{xsk,i}$	
	Upper	Lower	Upper	Lower
a_1	-1	0	-0.4	0
a_2	9.5	0	3.2	0.3
a_3	12	3	3.6	0.7
a_4	15.5	0	4.1	-0.3
a_5	22	-3	8.1	-3.1
a_6	27	-6	16.5	-9.6

Table 5
First round optimal results for the transonic case.

	Optimal parameters					
Upper surface	a1 0.005	a2 0.004477	a3 −0.00058	a4 0.003452	a5 0.002	a6 0.001
Lower surface	b1 0.005	b2 0.005	b3 −0.00233	b4 −0.00307	b5 0.001758	b6 0.000963
Optimal lift/drag ratio		by ROM 2.7424			by CFD 2.7686	

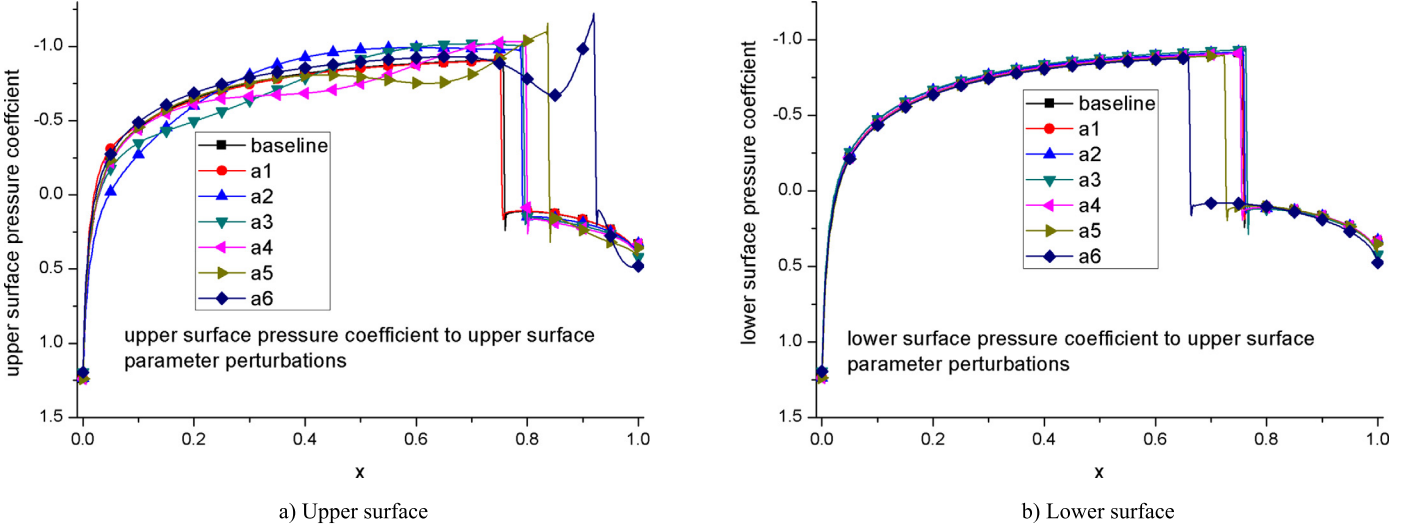


Fig. 22. Pressure coefficients of the upper surface perturbed for the transonic case.

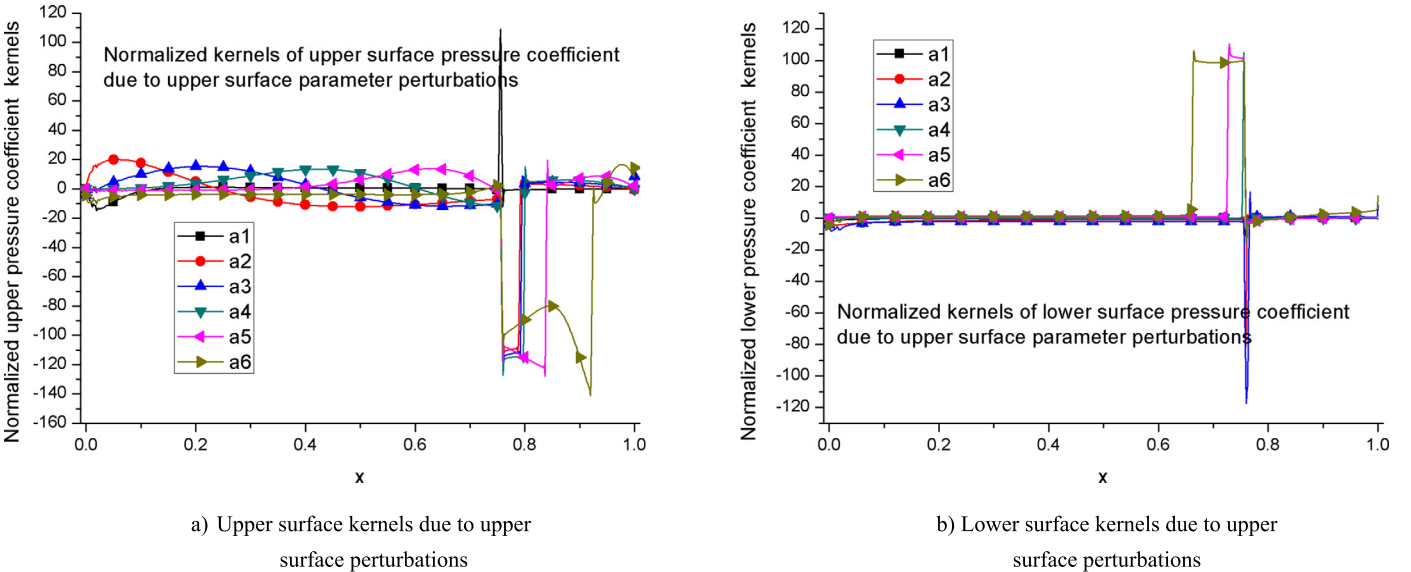


Fig. 23. Pressure kernels due to upper surface perturbations.

and b5, and $[−0.001, 0.001]$ for a6 and b6. The objective is set to $C_l / (0.05 + Cd)$. GA is used as optimization algorithm.

The optimal airfoil and pressure coefficients are shown in Fig. 28. The optimal parameters and lift-drag ratio are listed in Table 5. The lift-drag ratio of the optimized airfoil calculated by ROM is 2.7424, while the lift-drag ratio of the optimized airfoil calculated by CFD is 2.7686. Comparison between the pressures of the optimal airfoil (Fig. 28) calculated by the ROM and those calculated by the CFD indicates that the ROM results are acceptable. Therefore, the optimization method based on the ROM is feasible.

The number of iterations is 250 for the first round of optimization (Fig. 29). The time for this round is about 28 h which includes: the time of the baseline airfoil CFD analysis (4 h, one CFD simulation), the time of the CFD analyses for the six kernels (4 h each, six CFD simulations), and the time of GA optimization iteration (12 min for 250 iterations, no simulation). Furthermore, the CFD simulations are parallelly performed on several computers. If CFD were used in all 250 iterations, the total optimization time would be 1000 h. Therefore, the optimization efficiency is greatly improved.

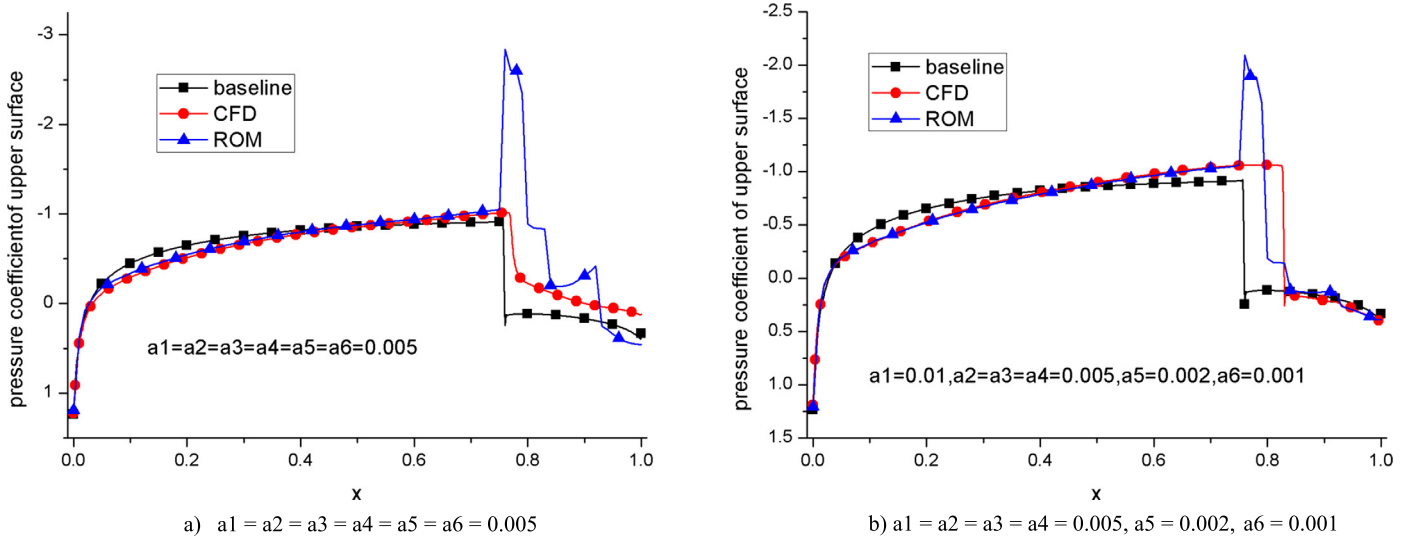


Fig. 24. Pressure coefficients predicted by ROM.

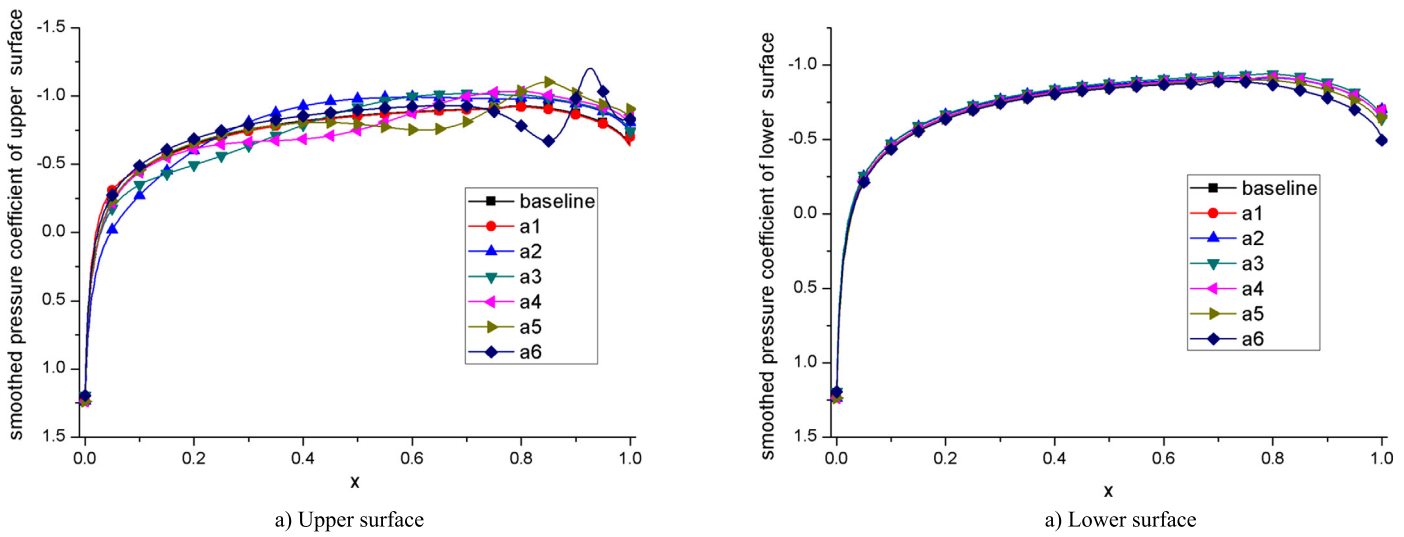


Fig. 25. Smoothed pressure coefficient of the disturbed airfoils.

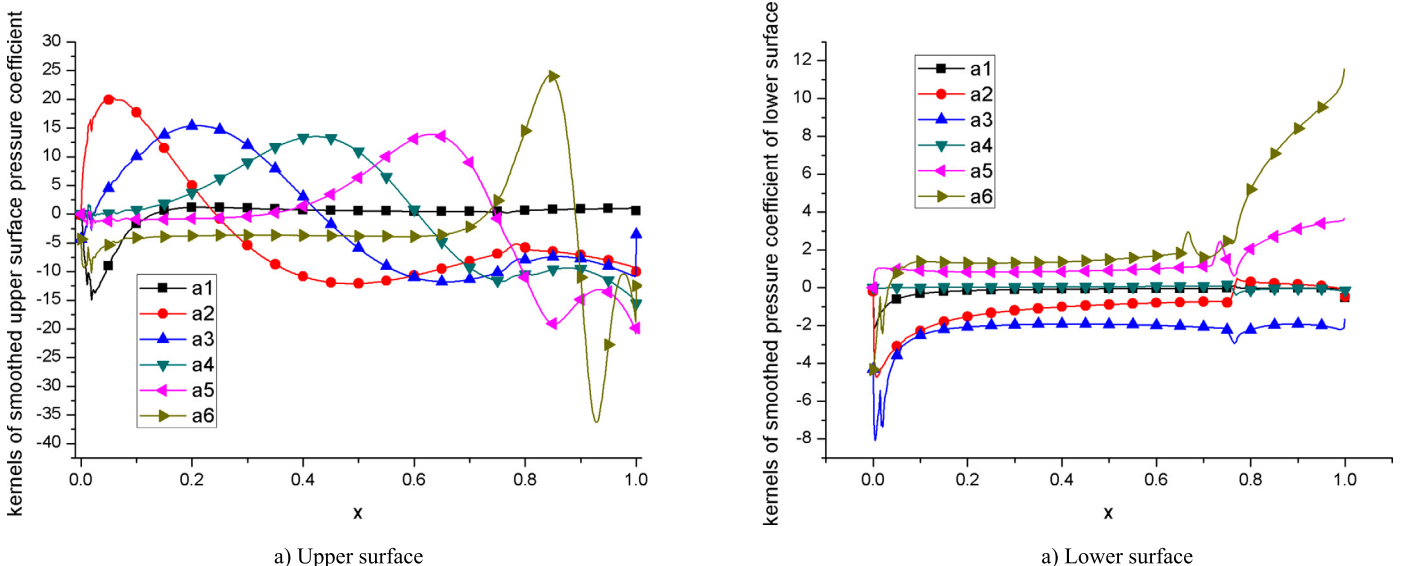


Fig. 26. Kernels of the smoothed pressure coefficient due to upper surface parameter changes.

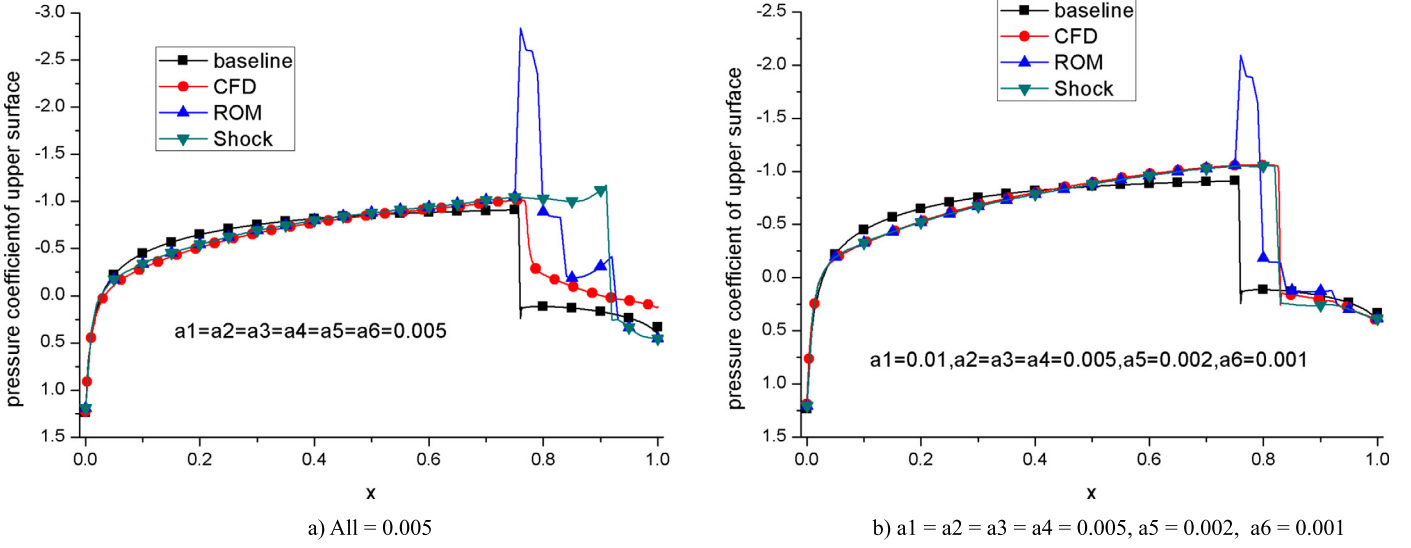


Fig. 27. Pressure calculated by the ROM considering shockwave.

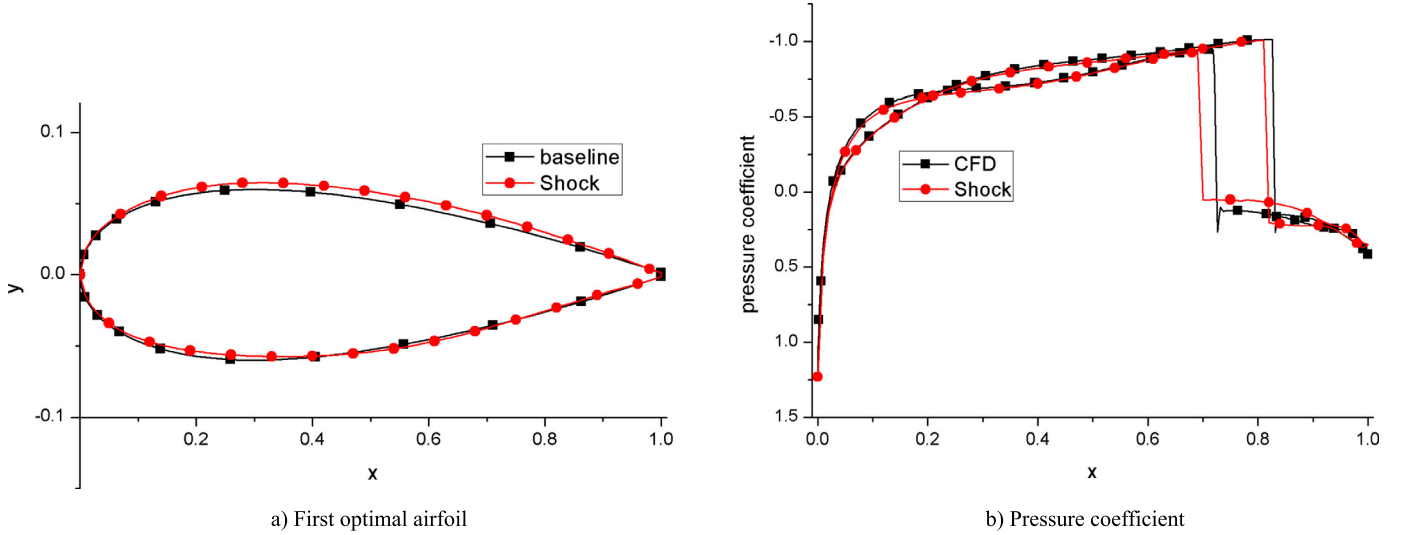


Fig. 28. First round optimization in the transonic case.

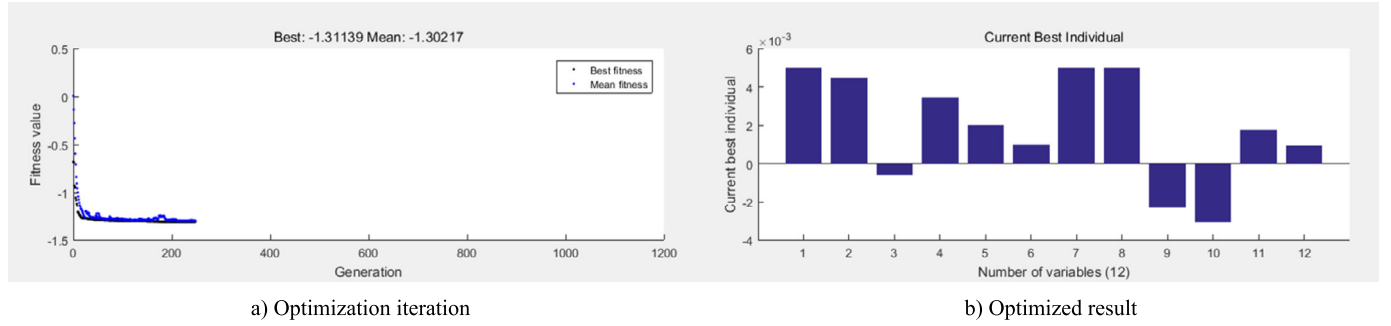


Fig. 29. First round optimization iteration in the transonic case.

4.4. Second optimization round of the transonic case

In the second optimization round, the optimal airfoil of the first round is used as the new baseline. The kernel data are updated, as shown in Fig. 30, as well as in Tables 6 and 7. The confidence ranges of the design parameters are $[-0.005, 0.005]$ for a_1-a_4 and b_1-b_4 , $[-0.002, 0.002]$ for a_5 and b_5 , and $[-0.001, 0.001]$ for a_6 and b_6 . The objective is $Cl / (0.05 + Cd)$.

Table 6

The shockwave pressure increment and shockwave position of the second baseline.

Pressure coefficient increment $\Delta p_{sk,0}$	Upper surface	1.175
	Lower surface	1.075
Shockwave position $x_{sk,0}$	Upper surface	0.829
	Lower surface	0.725

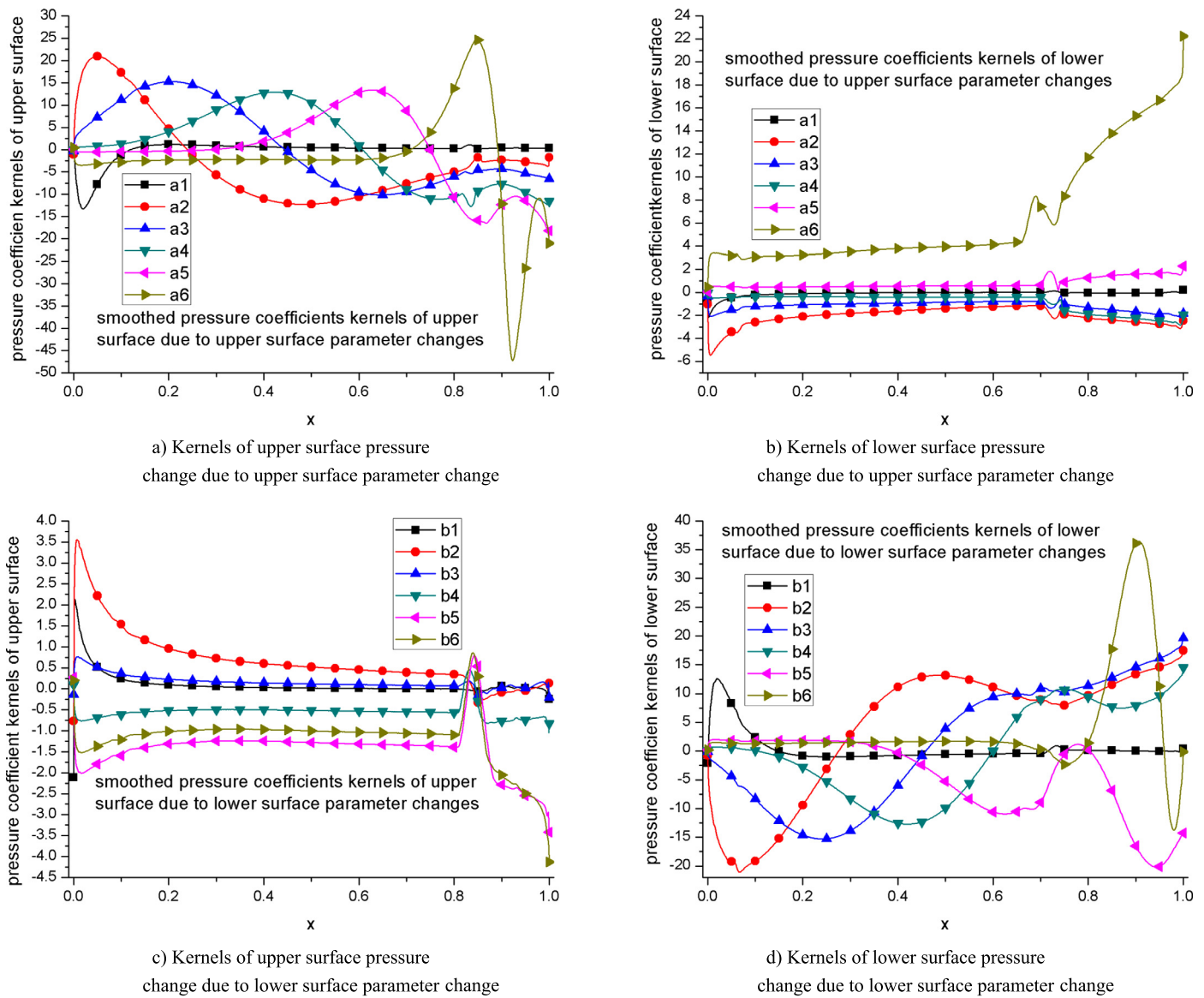


Fig. 30. Kernels of the smoothed pressure coefficients in the second round.

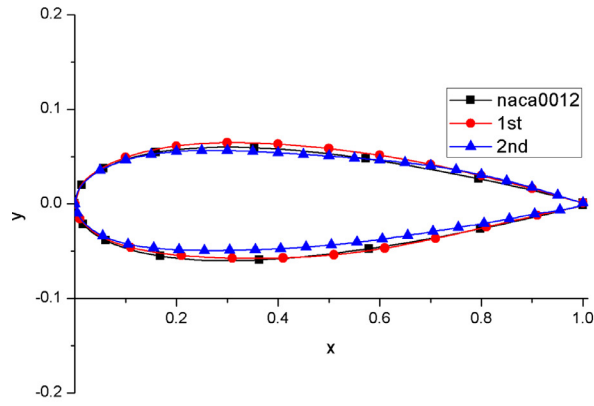
Table 7
Kernels of shockwave pressure increment and shockwave position in the second round.

Shape control parameter	Kernel of surface pressure coefficients increment $B_{sk,i}$		Kernel of surface shock position $B_{xsk,i}$	
	Upper	Lower	Upper	Lower
a1	-0.4	0	0	0
a2	3	2.6	2.4	0.8
a3	6	1.6	1.6	1
a4	12	2	0.6	0.8
a5	18	-1.6	4.8	-1.2
a6	28	-13.2	16.2	-9

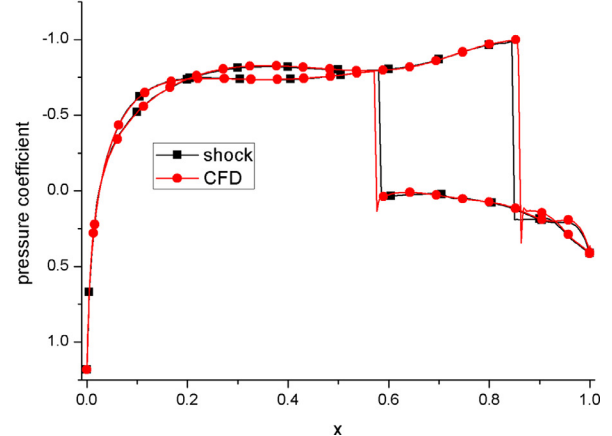
	Kernel of surface pressure coefficients increment $C_{sk,i}$		Kernel of surface shock position $C_{xsk,i}$	
	Upper	Lower	Upper	Lower
b1	0	0	0	-0.2
b2	0	-17	0	-5.6
b3	0	-19	0	-5.8
b4	0	-15	2.2	-8.6
b5	0	11	5.2	-9
b6	0	-3	4.6	-3.8

Table 8
Second round optima in the transonic case.

	Optimal parameters					
Upper surface	a1 -0.00478	a2 -0.00472	a3 -0.00498	a4 -5.48	a5 0.002	a6 8.66E-4
Lower surface	b1 0.005	b2 0.005	b3 0.003	b4 0.005	b5 0.002	b6 0.001
Optimal lift/drag ratio	by ROM 7.6070				by CFD 8.212	

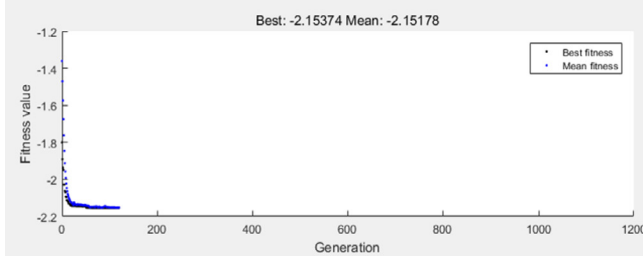


a) Airfoil

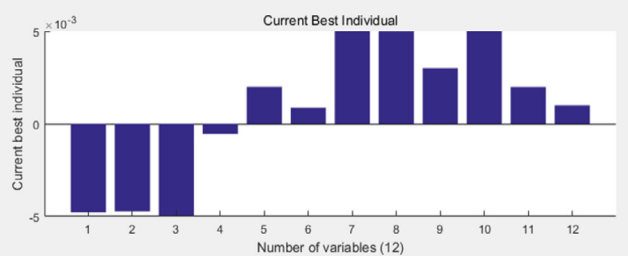


b) Pressure coefficient

Fig. 31. Second round optima for the transonic case.



a) Optimization iteration



b) Optimized result

Fig. 32. Second round iteration for the transonic case.

The optimal parameters and lift-drag ratio are shown in Table 8. The lift-drag ratio of the optimized airfoil calculated by the ROM is 7.607, while that ratio calculated by CFD is 8.212. The optimal airfoil is shown in Fig. 31a. Fig. 31b compares the pressures of the optimal airfoil (Fig. 28) calculated by the ROM and those calculated by the CFD, which indicates that their pressure coefficients are identical.

For this round, the total iteration number is 120 (Fig. 32). The total time is about 52 h which includes: the time of the baseline airfoil CFD analysis (4 h, one simulation), the time of the CFD analyses for the 12 kernels (4 h each, 12 simulations), and the time of the optimization iteration (12 min for 120 iterations, no simulation). Furthermore, the simulations are parallel performed on several computers. If CFD were used in all 120 iterations, the total optimization time would be 480 h. Therefore, the ROM method greatly improves the optimization efficiency.

4.5. Comparisons between the optimizations of the airfoils in subsonic and transonic flows

The optimizations of the airfoils in subsonic and transonic flows yield different trends (see Fig. 33). In the subsonic case, the airfoil

shape changes greatly and the airfoil curvature increases. The difference between the upper and lower surface pressures increases throughout the whole chord length.

In the transonic case, the airfoils shape changes around the trailing edge. The optimization mainly tends to move the upper surface's shockwave to the trailing edge and the lower surface's shockwave to the leading edge. The pressure difference between the upper and lower surfaces is induced by shockwave and the pressure difference between the upper and lower surfaces do not largely change before the shockwave.

5. Summary

To improve the accuracy and efficiency of the aerodynamic optimization, a multi-round optimization method is proposed based on a continually moving ROM. The optimization process is divided into several rounds, each of which uses the Hicks-Henne method to parameterize the airfoil. A local ROM, which uses the first order Taylor expansion, is built to predict the aerodynamic characteristics of the airfoil. To ensure the accuracy, the airfoil parameters are limited in the confidence space of each ROM during

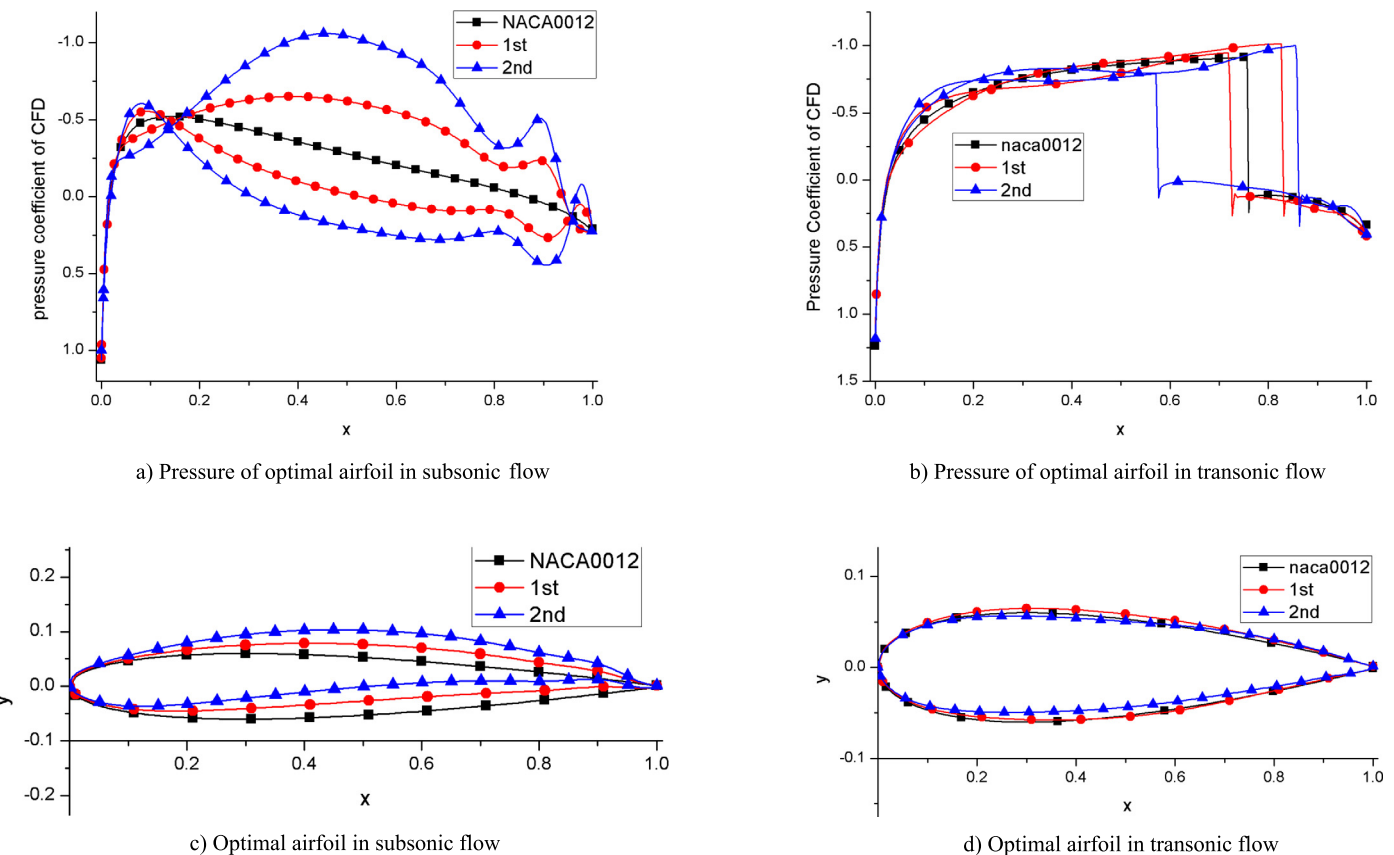


Fig. 33. Optimized airfoils for both subsonic and transonic flows.

the optimization. The ROM accuracy of each optimal airfoil is assessed at the end of each optimization round, and the confidence space is expended or narrowed accordingly. After that, the ROM moves to the obtained optimal point for the next round. The motion of the ROM in the design space ensures that the optimization explores the whole design space.

The NACA0012 airfoils in both subsonic and transonic flows are used to verify the optimization method. Under the subsonic flow condition, the lift-drag ratio increases from 0 to 25 by two rounds of optimization in this subsonic case. The total optimization time is 11 h which includes the time for two baseline airfoil CFD analyses, the time for 18 CFD analyses for kernels and the time for 446 optimization iterations. If CFD were used in all these optimization iterations, the total optimization time would be 223 h. Therefore, the optimization efficiency is greatly improved by the ROM method.

Additional consideration is included in the transonic flow ROM. In the ROM, the influence of airfoil shape perturbation on the aerodynamic force is divided into two parts, i.e. the smoothed part and the shockwave part. The smoothed part addresses the influence of the airfoil shape on the smooth aerodynamic force distribution. The shockwave part addresses the shockwave strength, the shock wave position, and their effects on the aerodynamic forces. By two rounds of optimization using ROM, the lift-drag ratio increases from 0 to 8 with 20 CFD simulations for ROM identification in the transonic case. The optimization efficiency is also greatly improved in this case.

The optimizations of the airfoils in subsonic and transonic flows yield different trends. For the subsonic case, the airfoil shape greatly changes and the airfoil curvature increases. The difference between the upper and lower surface pressures increases for the whole chord. For the transonic case, the airfoil shape changes around the trailing edge. The optimization mainly tends to move

the upper surface shockwave to the trailing edge and the lower surface shock wave to the leading edge. The pressure difference between the upper and lower surface is induced by the shockwaves. The pressures before the shockwaves do not largely change.

The impact of the confidential space size on the ROM accuracy is discussed. It is found that small shape disturbances have little effect on ROM accuracy. When the shape disturbance increases, the non-linear characteristics of the aerodynamic system emerge and the ROM results deviate from the CFD results.

Declaration of competing interest

The authors declare that they have no known competing financial interests or personal relationships that could have appeared to influence the work reported in this paper.

Acknowledgement

This project is supported by the National Science Foundation of China (No. 51775518).

The authors would like to express my gratitude to Professor X. M. Wang of Northwestern Polytechnic University in revising the manuscript and to the referees in their kindly suggestions.

References

- [1] M. Zhang, W. Gou, L. Li, F. Yang, Z.F. Yue, Multidisciplinary design and multi-objective optimization on guide fins of twin-web disk using Kriging surrogate model, *Struct. Multidiscip. Optim.* 55 (1) (2017) 361–373.
- [2] L. Li, J.K. Jiao, S.Y. Sun, Z.A. Zhao, J.L. Kang, Aerodynamic shape optimization of a single turbine stage based on parameterized free-form deformation with mapping design parameters, *Energy* 169 (2019) 444–455.
- [3] P.F. Wei, Z.Z. Lu, J.W. Song, Variable importance analysis: a comprehensive review, *Reliab. Eng. Syst. Saf.* 142 (2015) 399–432.

- [4] P.F. Wei, Y.Y. Wang, C.H. Tang, Time-variant global reliability sensitivity analysis of structures with both input random variables and stochastic processes, *Struct. Multidiscip. Optim.* 55 (5) (2017) 1883–1898.
- [5] P. Wang, Z.Z. Lu, K.C. Zhang, S.A. Xiao, Z.F. Yue, Copula-based decomposition approach for the derivative-based sensitivity of variance contributions with dependent variables, *Reliab. Eng. Syst. Saf.* 169 (2018) 437–450.
- [6] P. Wang, Z.Z. Lu, S.A. Xiao, A generalized separation for the variance contributions of input variables and their distribution parameters, *Appl. Math. Model.* 47 (2017) 381–399.
- [7] Y.S. Qiu, J.Q. Bai, N.L. Liu, C. Wang, Global aerodynamic design optimization based on data dimensionality reduction, *Chin. J. Aeronaut.* 31 (4) (2018) 643–659.
- [8] A. Da Ronch, M. Ghoreyshi, K.J. Badcock, On the generation of flight dynamics aerodynamic tables by computational fluid dynamics, *Prog. Aerosp. Sci.* 47 (2011) 597–620.
- [9] E. Iuliano, D. Quagliarella, Proper orthogonal decomposition, surrogate modeling and evolutionary optimization in aerodynamic design, *Comput. Fluids* 84 (2013) 327–350.
- [10] J.C. Li, J.S. Cai, K. Qu, Adjoint-based two-step optimization method using proper orthogonal decomposition and domain decomposition, *AIAA J.* 56 (3) (2018) 1133–1145.
- [11] D. Amsallem, M. Zahr, Y. Choi, C. Farhat, Design optimization using hyper-reduced-order models, *Struct. Multidiscip. Optim.* 51 (2015) 919–940.
- [12] R. Bourguet, M. Braza, A. Dervieux, Reduced-order modeling of transonic flows around an airfoil submitted to small deformations, *J. Comput. Phys.* 230 (1) (2011) 159–184.
- [13] G. Chen, D.F. Li, Q. Zhou, A. Da Ronch, Y.M. Li, Efficient aeroelastic reduced order model with global structural modifications, *Aerosp. Sci. Technol.* 76 (2018) 1–13.
- [14] K.C. Hall, E.F. Crawley, Calculation of unsteady flows in turbomachinery using the linearized Euler equations, *AIAA J.* 27 (6) (1989) 777–787.
- [15] K.C. Hall, C.B. Lorence, Calculation of three dimensional unsteady flows in turbomachinery using the linearized harmonic Euler equations, *ASME J. Turbomach.* 115 (4) (1993) 800–807.
- [16] W.S. Clark, K.C. Hall, A time-linearised Navier-Stokes analysis of stall flutter, *ASME J. Turbomach.* 122 (3) (2000) 467–476.
- [17] W.G. Yao, R.K. Jaiman, A harmonic balance technique for the reduced-order computation of vortex-induced vibration, *J. Fluids Struct.* 65 (2016) 313–332.
- [18] W.G. Yao, S. Marques, Application of a high-order CFD harmonic balance method to nonlinear aeroelasticity, *J. Fluids Struct.* 74 (2017) 427–444.
- [19] G. Dimitriadis, Continuation of higher-order harmonic balance solutions for nonlinear aeroelastic systems, *J. Aircr.* 45 (2) (2008) 523–537.
- [20] A.K. Gopinath, E. van der Weide, J.J. Alonso, A. Jameson, K. Ekici, K.C. Hall, Three-dimensional unsteady multi-stage turbomachinery simulations using the harmonic balance technique, *AIAA-2007-892*.
- [21] A. Rubino, M. Pinia, P. Colonna, Unsteady simulation of quasi-periodic flows in organic Rankine cycle cascades using a harmonic balance method, *Energy Proc.* 129 (2017) 1101–1108.
- [22] M.S. Campobasso, J. Drofelnik, F. Gigante, Comparative assessment of the harmonic balance Navier-Stokes technology for horizontal and vertical axis wind turbine aerodynamics, *Comput. Fluids* 136 (2016) 354–370.
- [23] L.Z. Li, J. Zhang, X. Luo, M.N. Yuan, X.M. Wang, An aerodynamic ROM of the blade subjected to wake based on Fourier method for flow, *Int. J. Numer. Methods Fluids* 89 (2019) 162–179.
- [24] H. Huang, K. Ekici, An efficient harmonic balance method for unsteady flows in cascades, *Aerosp. Sci. Technol.* 29 (2013) 144–145.
- [25] L. He, Harmonic solution of unsteady flow around blades with separation, *AIAA J.* 46 (6) (2008) 1299–1307.
- [26] L. He, Fourier methods for turbomachinery applications, *Prog. Aerosp. Sci.* 46 (2010) 329–341.
- [27] L.Z. Li, M.L. Yang, X. Luo, J. Zhang, M.N. Yuan, A spline ROM of blade aerodynamic force to upstream wake, *Aerosp. Sci. Technol.* 84 (2019) 650–660.
- [28] W.A. Silva, Reduced order models based on linear and nonlinear aerodynamic impulse responses, *AIAA-99-1262*.
- [29] D.E. Raveh, D.N. Mavris, Reduced-order models based on CFD impulse and step responses, *AIAA-2001-1527*.
- [30] R. Lind, R. Prazenica, M.J. Brenner, Estimating nonlinearity using Volterra kernels in feedback with linear models, *AIAA-2003-1406*.
- [31] M. Balajewicz, F. Nitsche, D. Feszy, Application of multi-input Volterra theory to nonlinear multi-degree of freedom aerodynamic systems, *AIAA J.* 48 (1) (2010) 56–62.
- [32] X.T. Li, Y.L. Liu, J.Q. Kou, W.W. Zhang, Reduced-order thrust modeling for an efficient flapping airfoil using system identification method, *J. Fluids Struct.* 69 (2017) 137–153.
- [33] D. Su, W. Zhang, M. Ma, Z. Ye, An efficient coupled method of cascade flutter investigation based on reduced order model, *AIAA-2013-3618*.
- [34] D. Su, W. Zhang, Z. Ye, A reduced order model for uncoupled and coupled cascade flutter analysis, *J. Fluids Struct.* 61 (2015) 410–430.
- [35] J.Q. Kou, W.W. Zhang, Multi-kernel neural networks for nonlinear unsteady aerodynamic reduced-order modeling, *Aerosp. Sci. Technol.* 67 (2017) 309–326.
- [36] G. Chen, Y.M. Li, Advances and prospects of the reduced order model for unsteady flow and its application, *Adv. Mech.* 41 (6) (2011) 686–701.
- [37] W.W. Zhang, K.J. Chen, Z.Y. Ye, Unsteady aerodynamic reduced-order modeling of an aeroelastic wing using arbitrary mode shapes, *J. Fluids Struct.* 58 (2015) 254–270.
- [38] Z.Y. Wang, W.W. Zhang, Unsteady aerodynamic reduced-order modeling method for parameter changeable structure, *Acta Aeronaut. Astronaut. Sin.* 38 (6) (2017) 173–182 (in Chinese).
- [39] M. Ghoreyshi, A. Jirasek, M. Cummings, Reduced order unsteady aerodynamic modeling for stability and control analysis using computational fluid dynamics, *Prog. Aerosp. Sci.* 71 (2014) 167–217.
- [40] A. Da Ronch, D. Vallespin, M. Ghoreyshi, K.J. Badcock, Evaluation of dynamic derivatives using computational fluid dynamics, *AIAA J.* 50 (2) (2012) 470–484.
- [41] A. Da Ronch, A.J. McCracken, K.J. Badcock, M. Widhalm, M.S. Campobasso, Linear frequency domain and harmonic balance predictions of dynamic derivatives, *J. Aircr.* 50 (3) (2013) 694–707.
- [42] A. Da Ronch, A. McCracken, K.J. Badcock, M. Ghoreyshi, R.M. Cummings, Modeling of unsteady aerodynamic loads, *AIAA-2011-6524*.
- [43] P.A. LeGresley, J.J. Alonso, Investigation of non-linear projection for POD based reduced order models for aerodynamics, *AIAA-2001-0926*.
- [44] J.Q. Luo, Design optimization of the last stage of a 4.5-stage compressor using a POD-based hybrid model, *Aerosp. Sci. Technol.* 76 (2018) 303–314.
- [45] X.J. Wu, W.W. Zhang, X.H. Peng, Z.Y. Wang, Benchmark aerodynamic shape optimization method with the POD-based CST airfoil parametric method, *Aerosp. Sci. Technol.* 84 (2019) 632–640.
- [46] P.A. LeGresley, J.J. Alonso, Dynamic domain decomposition and error correction for reduced order models, *AIAA-2003-0250*.
- [47] M.J. Zahr, C. Farhat, Progressive construction of a parametric reduced-order model for PDE-constrained optimization, *Int. J. Numer. Methods Eng.* 102 (5) (2014) 1111–1135.
- [48] Y.P. Liao, L. Liu, T. Long, The research on some parameterized methods for airfoil, *J. Project. Rockets Missiles Guid.* 31 (3) (2011) 160–164 (in Chinese).
- [49] A. Da Ronch, K.J. Badcock, Y. Wang, A. Wynn, R. Palacios, Nonlinear model reduction for flexible aircraft control design, *AIAA-2012-4404*.
- [50] B.M. Kulfan, Universal parametric geometry representation method, *J. Aircr.* 45 (1) (2008) 142–158.
- [51] G.D. Yang, A. Da Ronch, J. Drofelnik, Z.T. Xie, Sensitivity assessment of optimal solution in aerodynamic design optimization using SU2, *Aerosp. Sci. Technol.* 81 (2018) 362–374.